Laser and Particle Beams (2001), *19*, 355–376. Printed in the USA.

Plasma formation and the implosion phase of wire array *z*-pinch experiments

S.V. LEBEDEV,[1] F.N. BEG,[1] S.N. BLAND,[1] J.P. CHITTENDEN,[1] A.E. DANGOR,[1] M.G. HAINES,[1] S.A. PIKUZ,[2] AND T.A. SHELKOVENKO[2]

[1]The Blackett Laboratory, Imperial College, London SW7 2BW, United Kingdom
[2]P.N. Lebedev Physical Institute, Moscow 121433, Russia

(RECEIVED 22 May 2000; ACCEPTED 22 February 2001)

Abstract

Experiments to study plasma formation and implosion dynamics of wire array *z* pinches performed on MAGPIE generator (1.4 MA, 240 ns) at Imperial College are reviewed. Data from laser probing and X-ray radiography show that heterogeneous plasma structure with dense wire cores surrounded by low-density coronal plasma persists in wire arrays for a significant part of the implosion. Early implosion of the coronal plasma produces a precursor plasma column on the array axis, parameters of which depend on the rate of radiative cooling. The seeding of perturbations on the dense core of each wire is provided by nonuniform sweeping of the low-density coronal plasma from the cores by the global $\mathbf{J} \times \mathbf{B}$ force. The spatial scale of these perturbations (~0.5 mm for Al, ~0.25 mm for W) is determined by the size of the wire cores (~0.25 mm for Al, ~0.1 mm for W). A qualitative change in implosion dynamics, with transition to 0-D-like trajectory, was observed in Al arrays when the ratio of interwire gap to wire core size was decreased to ~3. In experiments with nested wire arrays, two different modes of operation were identified, both giving significant sharpening of the X-ray pulse (~10 ns) in comparison with a single array, despite the small number of wires in the arrays (16 outer, 16 inner) and the long implosion time (260 ns).

1. INTRODUCTION

Present levels of X-ray power and yield (280 TW, 4 ns, 1.8 MJ), achieved in wire array *z*-pinch implosions (Sanford *et al.*, 1996; Deeney *et al.*, 1997*a*; Matzen, 1997; Spielman *et al.*, 1998), make them of great interest for a number of applications including inertial confinement fusion (ICF), high energy density physics, and laboratory astrophysics. The parameters of the X-ray pulses generated at stagnation of the plasma on the axis are diagnosed in great detail on multi-megaampere facilities (9-MA Saturn and 20-MA Z) at Sandia National Laboratories (SNL). Significant success was achieved in development of 2-D magnetohydrodynamic (MHD) computer codes (modeling in the *r*–*z* plane; Peterson *et al.*, 1999; Douglas *et al.*, 2000), which are able to reproduce the shape and intensity of the X-ray pulses. This modeling shows that implosion quality is determined by the development of the Rayleigh–Taylor (R-T) instability in the plasma accelerated by the magnetic field. To reach agreement between the modeling and the X-ray pulse measured in experiments, the initial conditions for the simulations are adjusted by using artificially introduced random density perturbations. Experimentally, the initial conditions of the plasma, at the time of initiation of the model, are not known. Probably more important, the lack of experimental data does not allow verification that the modeling adequately describes the implosion, as only parameters of plasma at stagnation can be compared. This situation makes the problem of understanding the early (prestagnation) behavior of the plasma in wire array *z* pinches extremely important for further progress in the field.

The time history of plasma dynamics in a wire array implosion can be subdivided into several stages, as shown in Figure 1. The discharge starts from solid metallic wires, separated by a distance 20–100 times greater than their initial diameter. Fast rising current (~1 kA/ns per wire) rapidly heats the wires to the boiling temperature during the first few nanoseconds. There is strong experimental (Kalantar & Hammer, 1993; Deeney *et al.*, 1997*b*; Lebedev *et al.*, 1999; Pikuz *et al.*, 1999) and computational (Lindemuth, 1990; Chittenden *et al.*, 2000) evidence, that plasma produced in this process has a heterogeneous structure with dense cold cores surrounded by a low-density coronal plasma, which can be MHD unstable. Merging of low-density coronal plasma from different wires may occur early, while the dense wire cores may remain nonmerged for a much longer time. The acceleration of the coronal plasma by $\mathbf{J} \times \mathbf{B}$ force

Address correspondence and reprint requests: S.V. Lebedev, Blackett Laboratory, Imperial College, London SW7 2BW, UK. E-mail: s.lebedev@ic.ac.uk

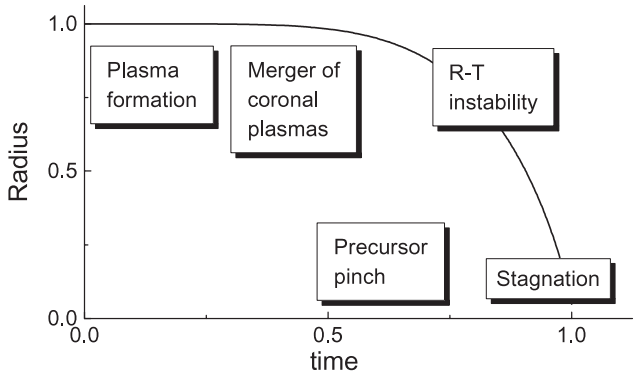

Fig. 1. A life history of wire array *z*-pinch implosion.

towards the array axis forms a precursor pinch before the main implosion. During these first stages, the discrete nature of the wires and the 3-D topology of the system are important, and they may determine the seed level of perturbations, which provide the initial conditions for the later growth of the R-T instability. The parameters of the plasma at stagnation (and the resulting X-ray pulse) should depend not only on the R-T growth, but also on the amount and radial distribution of the material streaming inward in the array (Whitney *et al.*, 1997) during the early stages of the wire array implosion history—the precursor plasma.

In this article we present a review of experiments performed on the MAGPIE facility (Mitchell *et al.*, 1996) at Imperial College, which were designed to study the physics of wire array *z*-pinch implosions. These experiments were carried out at 1–1.4 MA of current, which means that some care should be taken in scaling of the quantitative results to the higher currents, though we believe that the main features of the physical picture remain the same. The content of this article is as follows. In Section 2, we describe the experimental setup and diagnostics. Section 3 presents experimental data on plasma formation from individual wires in the array, which demonstrate that core–corona structure of plasma exists for up to 80% of the implosion. Data on formation of a precursor plasma column on the array axis are presented in Section 4. In Section 5, we describe measurements of instabilities which develop in individual wires of the array during the run-in phase of a *z*-pinch implosion. Comparison of the X-ray radiography data with simultaneously performed laser probing shows that instabilities, which are first seen in a low density coronal plasma around each wire, produce an imprint on the dense wire cores when the array starts to implode. These data show that streaming of the unstable coronal plasma from wire cores and associated axial nonuniformity of the core ablation could be primarily a mechanism for the seeding of perturbations in wire arrays. In Section 6, we present data on the development and structure of the global $m = 0$ mode of the R-T instability. In Section 7 we discuss the effect of wire number on the implosion dynamics and show that the implosion trajectory of wire cores deviates significantly from that predicted by the 0-D model if the number of wires in an array is less than some critical number. This critical number is determined by the ratio between interwire gap and the size of the core plasma associated with each wire. If this ratio becomes less than ~3, the array implodes following a 0-D (shell-like) trajectory, even without physical merging of wire cores. The inward streaming of the coronal plasma from the wires also stops at the same ratio of interwire gap to core size. Section 8 describes experiments with nested wire arrays, in which we identify two different dynamic modes of implosion. A significant sharpening of the X-ray pulse was obtained in both the modes, despite the small number of wires in the arrays, when implosion definitely cannot be described as the interaction of two colliding plasma shells. In particular, the mode with a fast switching of the current to the inner wire array (Davis *et al.*, 1997) provides very stable implosion of the inner array and promises favorable scaling to large diameter arrays. Finally, the main results are summarized in Section 9.

2. EXPERIMENTAL SETUP AND DIAGNOSTICS

The experiments were carried out on the MAGPIE (Mega Ampere Generator for Plasma Implosion Experiments) generator (Mitchell *et al.*, 1996) with current rising up to 1 or 1.4 MA in 240 ns (10% to 90% rise time is 150 ns). Figure 2 shows a schematic of the wire array load used in most of the experiments. The 1.6-cm-diameter, 2.3-cm-long annular wire array is mounted between the live cathode and the anode plate. Eight or four current-return posts are situated on a diameter of 15.5 cm. The design allows both end-on and side-on diagnosis of the whole array. Experiments were per-

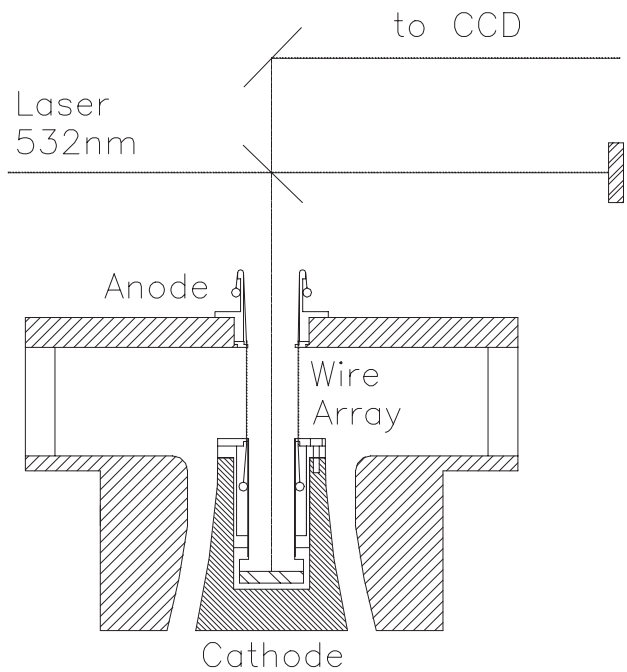

Fig. 2. Schematic of wire array load.

https://doi.org/10.1017/S0263034601193122 Published online by Cambridge University Press

formed with arrays of 8, 16, 32, and 64 Al, W, or Ti wires of different diameters (15 μm Al; 4, 5, and 7.5 μm W, and 20 μm Ti). The wires were positioned to an accuracy better than 0.2 mm and were kept in tension by weights attached to the ends of each wire. Due to the high impedance of the generator (1.25 Ω), the current waveform was relatively insensitive to the number of wires in the array. The implosion times for arrays with different number of wires were between 180 and 320 ns as determined from the onset of the kilovolt X-ray pulse from the pinch and from optical streak photographs.

In addition to "standard" cylindrical arrays, where wires are equally spaced, two other experimental configurations were used in some experiments. In the first (4×4 configuration), wires in the array were positioned in four groups with four closely spaced wires in each group (Lebedev *et al.*, 1999). This configuration preserves the main feature of the magnetic field topology, the existence of the $\mathbf{J} \times \mathbf{B}$ force, which blows off the low-density coronal plasma from the wires. At the same time, in this configuration it is possible to follow plasma formation for small interwire separation in the group for a longer time than in a cylindrical array, and also to measure radial structure of the imploding plasma. The second configuration used in experiments is a "twisted" wire array, in which a top electrode holding wires was rotated at an angle $\pi/4$, $3\pi/8$, or $\pi/2$. Small angles of rotation were used to measure azimuthally averaged radial distribution of the coronal plasma inside the array. For larger angles of rotation, the hourglass shape of the configuration offers a possible means for mitigation of R-T instability (Douglas *et al.*, 1997*a*). The B_z magnetic field, measured inside the twisted arrays in our experiments, provided information that the current path is not shunted by the merged coronal plasma, but is localized along the wire cores.

Diagnostics used in the experiments included laser probing, optical and soft X-ray imaging, different X-ray detectors, time- and space-resolved XUV spectroscopy, and X-ray radiography.

Optical probing was performed using a frequency doubled Nd-YAG laser (532 nm) with SBS pulse compression (0.4 ns), and images were recorded on CCD cameras. The laser beam was split to provide simultaneous end-on and side-on measurements. For the end-on laser probing, which gives information about the azimuthal structure of the implosion and about radial distribution of the coronal plasma, a mirror was installed deep inside the cathode (Fig. 2). During end-on probing, shadow and interferometer channels were registered simultaneously. The side-on optical diagnostics include laser probing with interferometer, shadow and schlieren channels, and a streak camera with its slit oriented along the array radius. The timing of the laser pulse was registered on the optical streak camera, which provided synchronization of optical streaks with other diagnostics. X-ray diagnostics include a gated 4-frame camera XRD diodes with Al photocathode and photoconducting detectors (PCD; Spielman *et al.*, 1997) with different filters. The

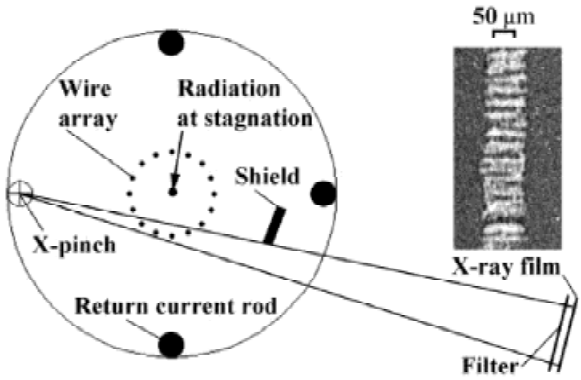

Fig. 3. Scheme of the experimental setup for X-ray radiography and radiographic image of 20-μm Ti wire in 16 wire array at 180 ns.

4-frame X-ray camera (2-ns gate, 9-ns frame separation) had a spatial resolution of 0.5 mm and, for measurements during the run-in phase of implosion, was filtered with 1.5- to 5-μm-thick polycarbonate (X-ray transmission window between 150 and 290 eV).

XUV spectroscopy in the range 5–40 nm was performed using a grating (glazing incidence) spectrometer. The spectra were recorded on a gated MCP camera, which provided temporal resolution of $\sim$10 ns. The use of an additional slit, which formed an image on the input slit of the spectrometer, provided spatial resolution of $\sim$0.5 mm in the radial direction, and spectra were recorded both side-on and end-on.

Point-projection X-ray radiography (Fig. 3) was performed using an *x* pinch installed in one of the four return current conductors. The timing of the backlighting X-ray pulse was adjusted by the use of different wire diameters (20–50 μm Al) and different numbers of wires (2–4) in the *x* pinch. This technique gave high spatial ($<$15 μm) and temporal ($\sim$1 ns) resolution and had been used previously in studies of single wire explosions (Shelkovenko *et al.*, 1999). The energy of the probing radiation hν $\sim$3–5 keV was determined by the emission spectrum of the *x* pinch (Shelkovenko *et al.*, 1999) and by transmission of the filter (12.5-μm-thick Ti) in front of the KODAK DEF film used for recording. The necessity to shield the film from the intense X-ray radiation generated at the stagnation of the array restricted the field of the view, and only $\sim$3 mm radially inwards from the array edge were recorded.

3. FORMATION OF PLASMA IN WIRE ARRAYS

Recent experimental data from single wire *z*-pinch explosions (Kalantar & Hammer, 1993; Pikuz *et al.*, 1999) and cold-start simulations (Lindemuth, 1990; Chittenden *et al.*, 2000, 2001) clearly show the formation of a heterogeneous plasma structure with a dense, cold-wire core, surrounded by a low-density coronal plasma. Very detailed information about the structure of the core, measured by a high-resolution X-ray backlighting technique can be found in Pikuz *et al.* (1999), Sinars *et al.* (2000), and Shelkovenko *et al.* (1999).

https://doi.org/10.1017/S0263034601193122 Published online by Cambridge University Press

In wire arrays, evidence of similar core–corona structure was detected by laser probing in experiments at current levels of 1 MA (Lebedev *et al.*, 1999) and 7 MA (Deeney *et al.*, 1997*b*). However, the formation of plasma in a wire array is expected to be significantly different from single-wire *z* pinches due to the net radially inward $\mathbf{J} \times \mathbf{B}$ force, which blows the coronal plasma from the wires to the array axis. This may strongly affect the rate of ablation of the wire cores and the character of perturbations in the wires (Chittenden *et al.*, 1999; Hammer & Ryutov, 1999). The fraction of total mass of the wires that is converted initially into the coronal plasma is small. This will result in rapid acceleration of this plasma from the wires to the array axis and the remaining wire cores will be exposed to the axial electric field induced due to change of the magnetic flux. It has been suggested (Hammer & Ryutov, 1999) that this would result in fast ionization of the wire cores and provide the means for the current to be concentrated in the cores. This is seemingly supported by the existing agreement between the experimentally measured implosion times, and those calculated from a 0-D model, which assumes that all of the initial mass implodes. However, until recently (Lebedev *et al.*, 2000*b*), there were no direct measurements of the conditions and the lifetime of the dense cores of wires in imploding wire arrays.

3.1. Core–corona structure of plasma

Direct evidence of the existence of the dense cores in wire array implosions was obtained in our experiments by using X-ray backlighting. Figures 4 and 3b show X-ray radiography images of the wires at the edge of wire array, obtained for Al and W, and Ti at early time (~60–70% of implosion time). The uniformity of wire cores on small spatial scales (comparable with the initial wire diameter) is different for different materials, similar to that observed in single-wire *z*-pinch explosions (Pikuz *et al.*, 1999; Sinars *et al.*, 2000). For example, Ti wires show a highly developed structure (Fig. 3b) with a typical spatial scale of 10–20 μm (for 20-μm initial wire diameter), while no small-scale structure is seen in Al wire cores. Existence of small-scale structures in wire cores can be expected for W, but at a spatial scale smaller than resolution in our experiments. At a longer spatial scale, the axial distribution of mass averaged over 0.2–0.5 mm is fairly uniform at this early time for both Al and W.

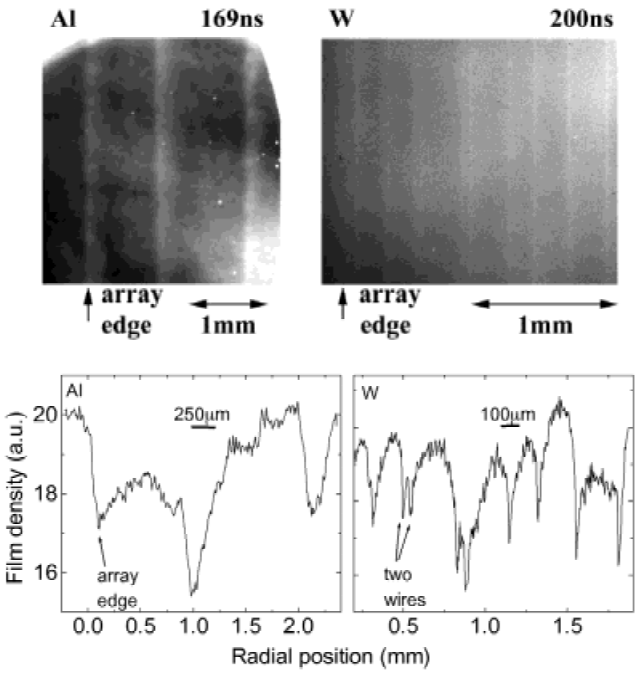

Fig. 4. Radiographic images of edge wires in Al and W arrays (top) and the corresponding radial profiles of film optical density (bottom).

The radiographic images shown in Figure 4 for Al and W were obtained at ~70% of the implosion time and the corresponding radial profiles of the optical density are presented in Figure 4c,d. From these data, the characteristic sizes of the wire cores are ~0.25 mm for Al and ~0.1 mm for W. These sizes are found to be the same for arrays with 16 and 64 wires, that is, insensitive to the current in each wire. The significant difference in the core size for Al and W strongly affects the implosion dynamics of the arrays, which will be discussed in Section 7. It is seen from Figure 4 that the expansion of the wire cores for both materials is not symmetric in the inward and outward radial directions of the array, with a sharper boundary on the outer radius. A slower fall-off in the inward radial direction indicates streaming of wire material to the array axis, in agreement with laser probing data, which show inward motion of the coronal plasma (Lebedev *et al.*, 1999).

Images of the arrays obtained in side-on laser probing show that strong azimuthal mass modulation persists for a long time (similar to Fig. 5). The existence of wire cores in the initial positions of wires is seen in both X-ray radiography and laser probing for ~80% of the implosion; this agrees with data obtained by optical streak photography, which shows optical emission from the initial position of wires until the same time. Characteristic density of the coronal plasma around the cores was measured by interferometry. A typical side-on interferogram taken from an array with 16 wires at 120 ns (half of the implosion time) is shown in Figure 5. The interference fringes between the wires are visible up to a distance of about 0.3 mm from the wire center. For the wires near the center of the array, measurement of the interference fringes shift yields the distribution of $\langle n_e l \rangle$ *versus* distance from the wire position (Fig. 5b), the maximum value being 3×10^{17} cm^{-2} at 0.3 mm from the wire center. From this plot, by integrating the $\langle n_e l \rangle$ distribution, the line density in the coronal plasma N_e is $\sim 2 \times 10^{16}$ cm^{-1}, which corresponds to ~20% of the initial wire mass if it is singly ionized. However, results of two-dimensional MHD simulations of the single Al wires pinches (Chittenden *et al.*, 2000, 2001) suggest that the coronal plasma is of high temperature (~30 eV) and has an ion charge of ~5–6. This would decrease the previous mass estimate to ~3%.

https://doi.org/10.1017/S0263034601193122 Published online by Cambridge University Press

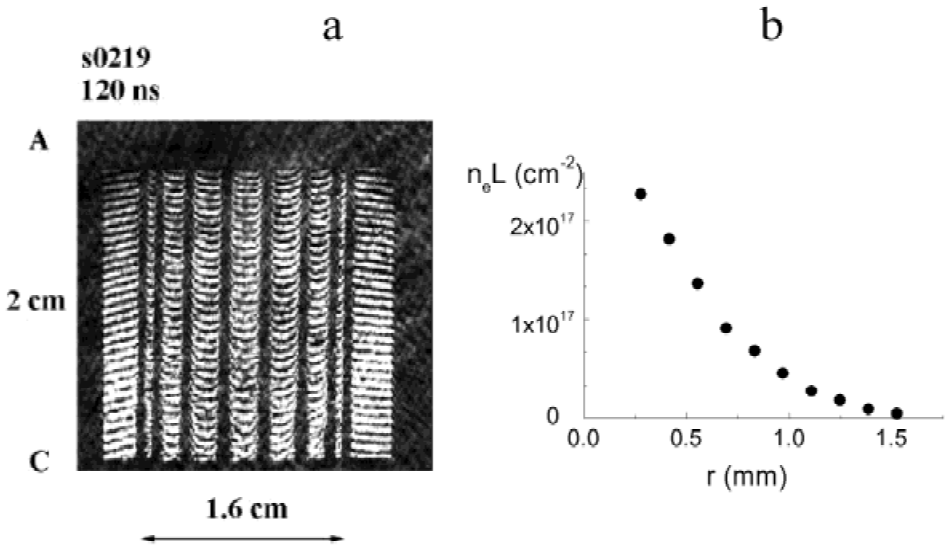

Fig. 5. Interferometer side-on image of the array (a) and n_eL *versus* distance from the wire position (b).

3.2. Inward streaming of the coronal plasma

The process of early acceleration of the coronal plasma to the array axis is most clearly seen from end-on laser probing data (Lebedev *et al.*, 1998, 1999). Figure 6 shows typical end-on laser interferograms obtained for different wire materials. It is seen that for arrays with large interwire gaps, the coronal plasma accelerates separately from each wire and only merges closer to the array axis. Figure 6a shows an end-on interferogram and a shadowgram for a 16 Al wire array. A fringe shift of 1 fringe corresponds to an electron number density of 9.1×10^{16} cm^{-3} for a probing path parallel to the pinch axis of 2×2.3 cm long. At times less than 60 ns, the plasma density inside the array is below the sensitivity of the interferometer ($n_e < 3 \times 10^{16}$ cm^{-3}). After this time, the plasma is observed inside the array in the form of radially directed streams. The plasma with the highest density is located around the initial positions of wires, where due to refraction, the probing laser beam is deflected out of the optical system. Outside these regions, the plasma den-

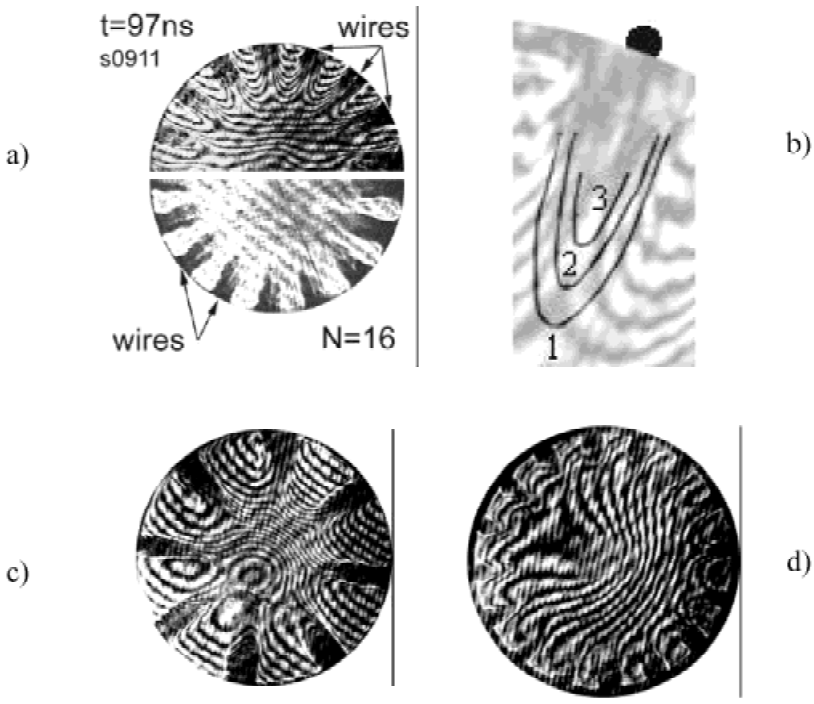

Fig. 6. End-on laser probing of the coronal plasma in wire arrays. (a) Interferogram (top) and shadowgram (bottom) of 16 Al wire array and the electron number density contours (b) corresponding to multiples of $n_e = 9 \times 10^{16}$ cm^{-3}. Interferograms of 8 Ti (20 μm) wire array (c) at $t = 92$ ns and 16 W (4 μm) wire array (d) at $t = 124$ ns.

https://doi.org/10.1017/S0263034601193122 Published online by Cambridge University Press

sity gradients are lower and a shift of interference fringes can be measured. Figure 6b shows a magnified part of the interferogram together with contours of electron number density. The total line density of electrons (N_e) inside the array found by integrating this density distribution is $N_e \sim 1.5 \times 10^{17}$ cm^{-1}. Using an ion charge of ~6, which is supported by both XUV spectroscopy data (as discussed later in this section) and by two-dimensional MHD simulations (Chittenden *et al.*, 2000), yields a mass estimate of ~2% for the fraction of coronal plasma inside the array at this time.

From a comparison of the interferograms obtained at different times, it is possible to find the inward radial velocity of the coronal plasma. The measured radial position of the plasma with $n_e \sim 10^{17}$ cm^{-3} *versus* time for Al arrays with 8, 16, and 32 wires is shown in Figure 7. It is seen that after 60 ns, the coronal plasma is moving with typical velocity of ~15 cm/μs and reaches the array axis at 120 ns, at about half of the implosion time. The 60-ns delay in the inward plasma motion agrees with the observed "dwell time" of the plasma expansion seen from side-on laser probing (Lebedev *et al.*, 1999). The shape of the density contours and their evolution in time show that this low-density coronal plasma expands 4–5 times faster in the inward radial direction than in the azimuthal. The faster radial motion is due to the $\mathbf{J} \times \mathbf{B}$ force provided by the global magnetic field of the array which is confirmed by observations made on arrays with one missing wire, where the directions of the plasma streams from the wires follow the topology of the global magnetic field. Assuming that the magnetic field does not affect the azimuthal expansion inside the array and that this occurs with the ion sound speed $C_s = (ZT_e/m_i)^{1/2}$, an estimate of the electron temperature can be obtained. For a measured velocity of about 3×10^6 cm/s this gives $ZT_e \sim 250$ eV, which is consistent with an equilibrium ionization state $Z = 6$ of the coronal plasma at $T_e \sim 40$ eV and $n_e \sim 10^{17}$ cm^{-3}.

These estimates of Z and T_e are in agreement with data from XUV spectroscopy. Figure 8 shows a typical spectrum of an Al wire array at $t = 150$ ns, which is spatially resolved

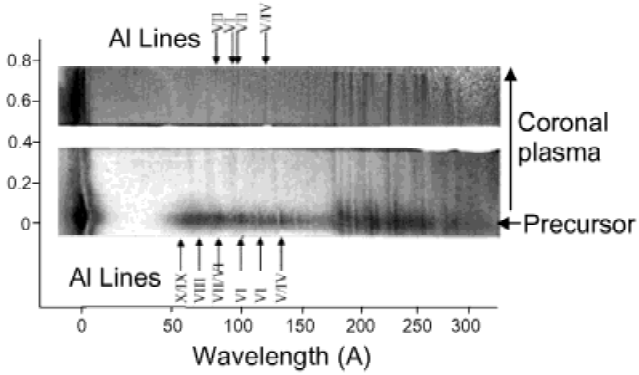

Fig. 8. Side-on spatially resolved XUV spectra Al wire array at $t = 160$ ns. Intense continuum radiation on the array axis is from the precursor pinch.

along the array radius. The intense continuum emission on the array axis from the region of ~1 mm in diameter is produced by the precursor pinch (see later in Sect. 4). At larger radii, where only emission from the wires is seen, spectral lines of Al ions with $Z = 5$ and 6 were identified.

For Al wire arrays with 32 and 64 wires, the merging of the coronal plasmas occurs much earlier, and the azimuthal structure of the plasma inside the array is formed by multiple collisions of the plasma streams from different wires (Fig. 9). The formation of the shocks is consistent with the small mean free path (m.f.p.) of Al ions. An estimate of m.f.p. for ion–ion collisions gives $\lambda_{ii} < 1$ mm (assuming $Z = 6$ and taking $n_e \sim 10^{17}$ cm^{-3} from the interferogram). The use of twisted wire arrays effectively removes the azimuthal structures (shocks) formed by collision of the streams from interferograms. These are not seen in this case due to averaging of the gradients along the probing path of the laser beam. The interferogram in Figure 10a, obtained for a 32 Al wire array at $t = 112$ ns, shows the distribution of the plasma inside the array for this configuration. The radial profile of the electron density obtained from this interferogram is shown in Figure 10b, where it was assumed that the fringe shift is zero at radius 0.2 cm, thus giving a lower estimate of the electron density. Integration of this density distribution

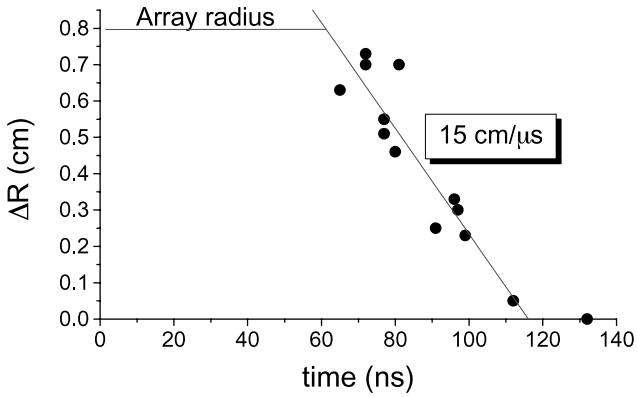

Fig. 7. Radial position of the coronal plasma boundary *versus* time, measured in Al wire arrays by end-on laser probing.

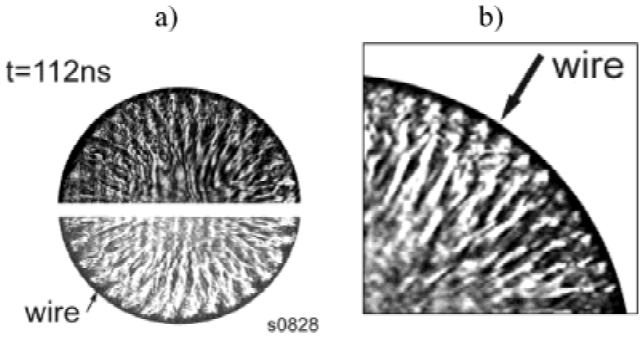

Fig. 9. End-on laser probing of 32 (a) and 64 (b) Al wires, showing collision of plasma streams from the neighboring wires.

https://doi.org/10.1017/S0263034601193122 Published online by Cambridge University Press

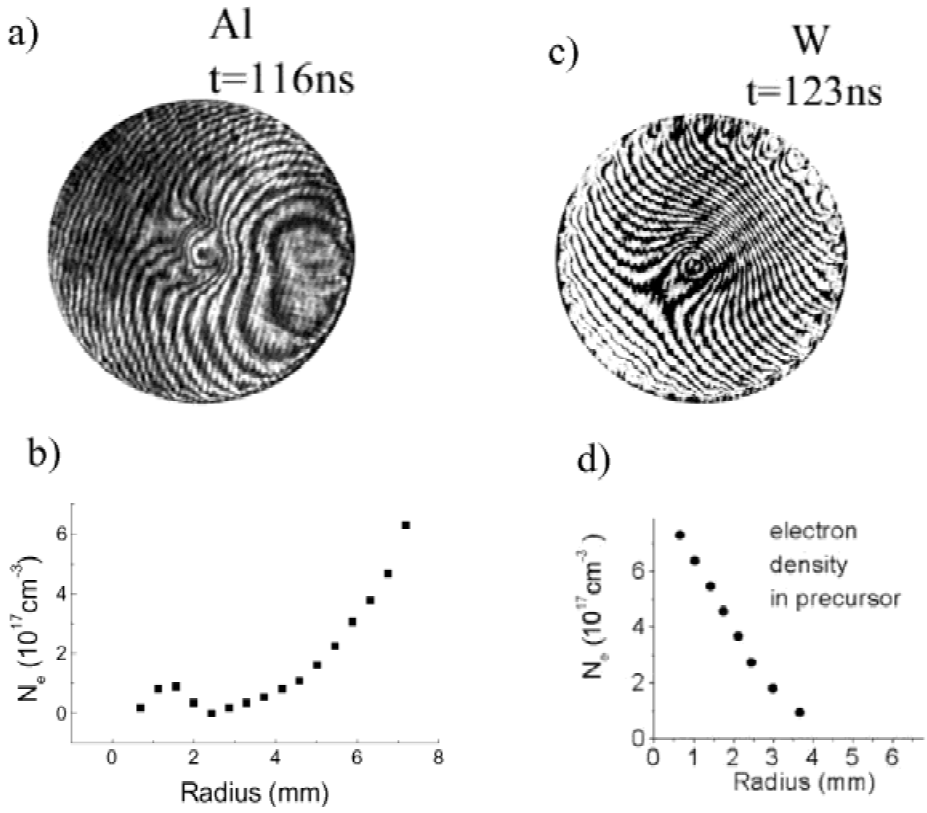

Fig. 10. End-on probing of twisted (by angle $\pi/4$) 32 Al wire array (a) and a cylindrical 32 W (c) wire array and the corresponding radial distributions (b,d) of electron number densities.

gives a total number of electrons inside the array $N_e = 4 \times 10^{17}$ cm^{-1}, which accounts for about 2% of the array mass (if $Z = 6$, as before).

To summarize, the end-on laser probing of Al wire arrays show that coronal plasma with electron density of $\sim 10^{17}$–10^{18} cm^{-3} fills the interior of the array at early times. Similar dynamics of the inward streaming of the coronal plasma is observed for arrays made of other materials (compare Fig. 6a,b,c).

For tungsten wire arrays (Fig. 10c,d), it is seen that plasma arrives on the array axis at ~100–120 ns, the same time as for Al. The azimuthal structure of the plasma inside the tungsten wire array, however, is significantly different from that in aluminum arrays. The separate streams of plasma are only seen near the initial positions of the wires. For smaller radii, closer to the array axis, distribution of the electron density is azimuthally uniform. This is due to a much higher kinetic energy of W ions (for about the same inward radial velocity), which results in a longer mean free path of the W ions, and in a collisionless character of the interaction of the plasma streams inside the array at these early times. Indeed, from the time of the plasma arrival at the axis, the velocity of the tungsten ions is $\sim(1\text{–}1.5) \times 10^7$ cm/s, which corresponds to the kinetic energy of W ions 10–20 keV, and the m.f.p estimate for the electron density shown in Figure 10d gives $\lambda_{ii} \sim 20$ mm (assuming an ion charge $Z \sim 15$).

Arrival of the coronal plasma on the array axis results in formation of the precursor pinch, which will be described in the next section.

4. PRECURSOR PINCH IN WIRE ARRAYS

A precursor pinch is formed in wire arrays when the coronal plasma, accelerated by the $\mathbf{J} \times \mathbf{B}$ force, stagnates on the array axis. For arrays with a small number of wires, the precursor pinch was detected in earlier experiments (Aivazov *et al.*, 1988; Deeney *et al.*, 1995; Yadlowsky *et al.*, 1996). The high kinetic energy of the ions in the plasma flow that forms the precursor results in a relatively high temperature of the precursor, which is evident from the observed soft X-ray emission. For arrays made of various wire materials the mechanism of precursor formation is the same, but the initial stages can be significantly different due to different collisionallity. This is demonstrated by the data obtained for Al and W wire arrays in our experiments.

4.1. Experimental data

Formation of the precursor pinch is seen most clearly from radial optical streaks, an example of which is shown in Figure 11 for a W wire array. For Al wire arrays an optical emission on the array axis starts at 120–140 ns (Lebedev *et al.*, 1999), and the time of the start of the precursor emis-

https://doi.org/10.1017/S0263034601193122 Published online by Cambridge University Press

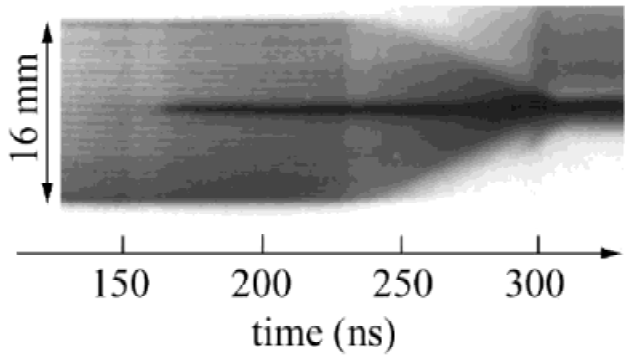

Fig. 11. Radial optical streak showing implosion dynamics and emission from precursor pinch on array axis in 64 W (4 μm) wire array.

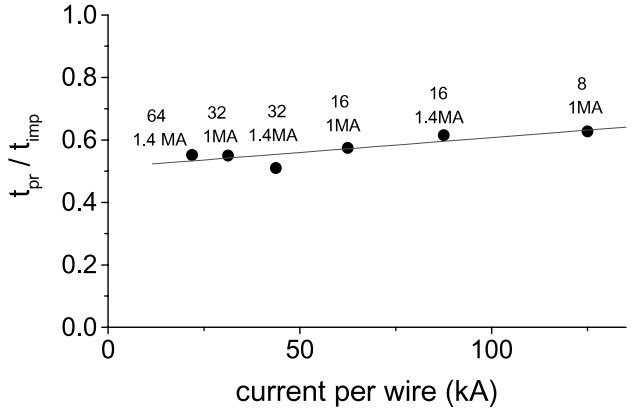

Fig. 12. Time of the start of optical emission from precursor in Al wire arrays with different wire number.

sion in Al arrays with different wire number is shown in Figure 12. The precursor formation time is almost identical for different numbers of wires and agrees well with the inward velocity of ~15 cm/μs of the low density coronal plasma, found from end-on laser probing measurements, and with the observed 60-ns delay in the start of this fast motion of the coronal plasma (see Fig. 7). The emission is observed from a well-defined region of about 1 mm in diameter, which is practically constant in time. For arrays with a small number of wires, the emission lasts until the implosion of the main mass of the array, while for an Al array with 64 wires, the emission from the precursor disappears at about 200 ns. This decay of precursor emission for 64 Al wire array (which is also seen in gated soft X-ray images) indicates a decrease of the flux of the coronal plasma from wires in this case (an effective plasma merger), which will be discussed in more detail in Section 7.

For Al wire arrays, laser probing starts to show the precursor from the same time as optical streaks. The interferogram in Figure 13a was obtained just after precursor formation (126 ns). The maximum density found from Abel inversion is 5×10^{18} cm^{-3} and the precursor pinch diameter measured at half of the density maximum is 0.6 mm. The precursor pinch column is observed on interferograms almost until the wires implode, but later in time the density gradients are higher and a fringe shift cannot be measured in the precursor center due to refraction of the probing laser beam. However, laser probing at later time show that the precursor diameter does not increase significantly.

Schlieren images (similar to that shown in Fig. 13c for W) show that the precursor plasma column is quite uniform in the axial direction despite the axial nonuniformity of the streams which form the precursor. The density of the precursor plasma in Al wire arrays, estimated from the sensitivity of the schlieren system (2×10^{-3} rad) agrees with interferometric measurements and for later times (~150 ns) gives $n_e \sim$ (1–2) $\times 10^{19}$ cm^{-3}. The line density of the precursor at this time for arrays with 16 wires is $N_e \sim 2 \times 10^{17}$ cm^{-1}. This gives an estimate of the precursor mass being ~1–2% of the total load mass, assuming an ion charge of Z = 5–10. This assumption about ion charge does not contradict the observed soft X-ray (200–300 eV) emission from the precursor and is supported by the observation of spectral lines of Al^{+7} ions in XUV spectra.

On gated soft X-ray images (Fig. 14b) the precursor in Al arrays is observed from ~110 ns until the stagnation of the array, as a homogeneous plasma column with a diameter of about 1 mm. The kinetic energy of the aluminum ions arriving at the axis, calculated from measured velocity of the coronal plasma is ~3 keV. Thermalization of this kinetic energy at stagnation and equipartition with electrons should result in a relatively high temperature of the precursor plasma, as supported by X-ray gated images which are recorded with a 5-μm-thick polycarbonate filter, transmitting photons with energy more than ~200 eV. End-on gated soft X-ray images (Fig. 15) also show formation of the precursor column, as well as at later time emission from the plasma streaming from the wire cores. It is seen from both side-on and end-on measurements that the precursor pinch persists for a long time, indeed until the implosion of the array. The radius of the precursor in Al reaches ~1 mm in 10–20 ns after the plasma first reaches the axis, and then the precursor radius is constant or only slowly increases in time at a rate of no more than 2×10^6 cm/s. If we assume that the increases of the precursor radius in time occurs with the ion sound speed, an estimate of the temperature gives $ZT \sim 100$ eV, which corresponds to an equilibrium ionization state of $Z \sim 6$ and $T \sim$ 15 eV. However, the mechanism of precursor plasma formation from the streams of energetic ions and the observed X-ray emission in the ~200-eV energy range indicate the possibility of a significantly higher plasma temperature. The experimental fact that the radius of the precursor is practically constant in time requires that some mechanism for confinement of the precursor plasma should be in place, which will be discussed later in this section.

For W wire arrays, the flux of coronal plasma from the wires also results in the formation of a precursor pinch. However, the initial stage of formation and the equilibrium diameter of the precursor are significantly different from the

https://doi.org/10.1017/S0263034601193122 Published online by Cambridge University Press

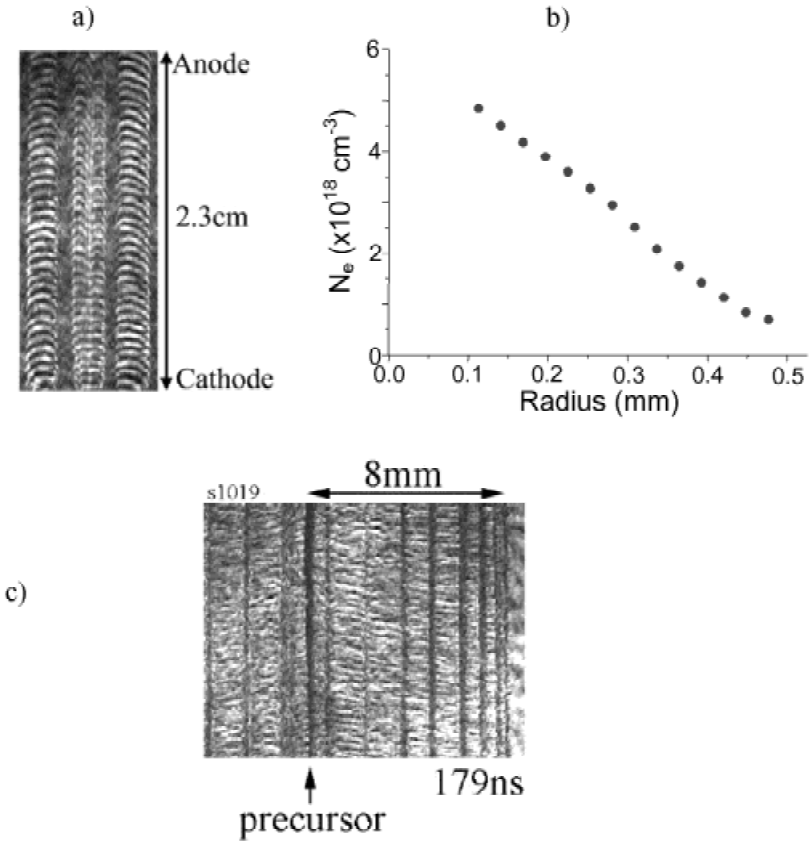

Fig. 13. Side-on interferogram (a) of the precursor pinch in 16 Al (15 μm) wire array at t = 126 ns and the corresponding radial profile of electron number density (b), and Schlieren image of the precursor pinch in W (c) wire array.

case of Al arrays. From end-on laser probing, described in Section 3, it was found that the coronal plasma reaches the axis at about the same time for both materials. A higher kinetic energy of the tungsten ions means that the plasma streams inside the array, including the region near the axis, are collisionless. This results in axially symmetric distribution of the tungsten ions with a smooth maximum at the array axis (see Fig. 10). The characteristic diameter of this distribution (at half maximum) is about 4 mm ($\frac{1}{4}$ of the array diameter), which is consistent with velocity spread in the plasma streams $V_\theta/V_r \sim \frac{1}{4}-\frac{1}{5}$ (which is similar to that measured for Al wire arrays). Continued injection of the plasma from the wires should gradually increase the density, which will result in a higher collisionallity of the system. This will also increase both the rate of energy transfer from ions to electrons and the rate of energy loss through radiation. In experiments, it is observed that after about 50 ns from the first arrival of the plasma on the axis, a dense and very narrow precursor plasma column is suddenly (in less than 10 ns) formed in tungsten wire arrays. This is seen at the same time in optical streaks (Fig. 11), from side-on laser probing (Fig. 13), and in gated soft X-ray images (Fig. 14). The typical diameter of this dense region is less than ~0.2 mm, which is 80 times smaller than the array diameter.

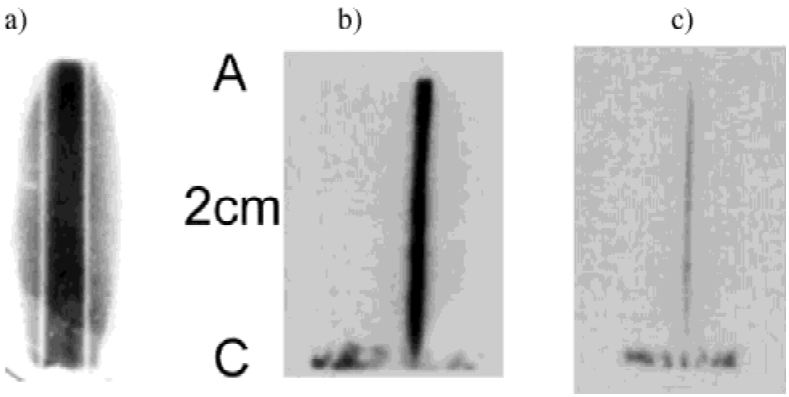

Fig. 14. Gated soft X-ray images of precursor in carbon (a), Al (b), and W (c) wire arrays.

https://doi.org/10.1017/S0263034601193122 Published online by Cambridge University Press

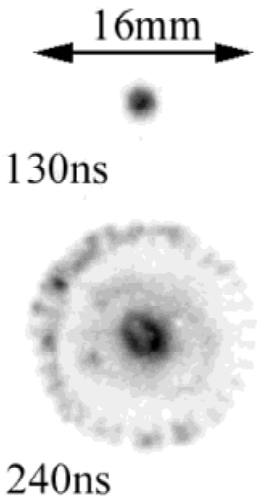

Fig. 15. End-on gated soft X-ray images of precursor formation in Al wire arrays.

Such a high compression ratio is difficult to explain simply by radial convergence of the plasma flow. Most probably, the gradual increase of the density (and the rate of radiation loss, $\sim n^2$) above some threshold triggers radiative instability (collapse) in the plasma, in analogy to that recently observed in experiments with laser-produced colliding plasmas (Farley *et al.*, 1999). After formation, the diameter of this narrow plasma column remains roughly constant in time, and the optical and soft X-ray emission from the precursor lasts until the main implosion occurs, that is, for about 50–150 ns for all wire numbers in tungsten wire arrays used in the present experiments.

4.2. Energy and pressure balance in the precursor

The strong dependence of the precursor diameter upon the atomic number, found in our experiments (~3 mm for C, ~1.5 mm for Al, ~0.2 mm for W; see Fig. 14), suggests that radiative cooling plays an important role in the dynamics of the precursor. The importance of radiation loss is further supported by the fact that the measured radiation power from the precursor is comparable to the flux of kinetic energy in the radial flow of the coronal plasma which forms the precursor. Full analysis of the precursor dynamics should include detailed modeling of radiation loss and is not yet available. Here we will consider a simple 0-D model, in which the precursor pinch has an equilibrium (constant in time) radius R, ion charge Z and temperature T, and is in pressure balance with the incoming flux of the coronal plasma. We will also assume that all kinetic energy of ions (E_i) in the incoming plasma flux is radiated (which assumes that the electron temperature is "frozen" at $T \ll E_i/(Z+1)$), and only the density of ions in the precursor $n_i(t)$ is increasing with time.

Assumption that all kinetic energy is radiated, allows us to find a lower estimate of the rate of mass accumulation in the precursor, if the total power of radiation from the precursor is measured. Indeed, the rate of mass accumulation can be written as

$$\frac{dm}{dt} = m_i n v 2\pi RL, \tag{1}$$

where m_i and v are ion mass and the radial plasma velocity, respectively, and L is the total length of the precursor. The flux of kinetic energy in the plasma flow at the boundary of the precursor, which we assume to be equal to radiation power, is equal to

$$Q_{rad} = E_i n v 2\pi RL. \tag{2}$$

Combination of Eqs. (1) and (2) gives an expression for the accumulation rate of mass in the precursor:

$$\frac{dm}{dt} = m_i \cdot \frac{Q_{rad}}{E_i}. \tag{3}$$

If the radiation loss is not the only sink for the kinetic energy of ions, a larger flux of ions is required to provide the measured radiation power, which means that this is a lower estimate of the mass flow in the precursor.

The absolute intensity of radiation from the precursor, measured by an unfiltered PCD detector for a 16 Al wire array, is shown in Figure 16. The use of this radiation power in Eq. (3) allows us to find the mass accumulated in the precursor (shown in Fig. 16b), as the kinetic energy of Al ions is known from the end-on laser probing measurements of plasma velocity. The velocity of ions in the calculation was assumed to be constant in time, which is consistent with the constant in time "hardness" of the measured soft X-ray emission from the precursor. The calculated mass of the precursor is in good agreement with measurements by laser probing at early time (see earlier in this section), both giving a mass fraction of ~2% at ~150 ns, and in agreement with 2-D (x–y plane) MHD simulations (Chittenden *et al.*, 1999, 2001). Later, at ~80% of the implosion time, the calculated mass in the precursor is about 5% of the array mass.

The obtained estimate of the mass accumulated in the precursor pinch can also be considered as an estimate of the mass ablated from the wires, taking into account a time delay of ~60 ns, required for the ions to reach the array axis. Later, in Section 7, we will use this in the analysis of implosion dynamics of wire cores.

This estimate of the mass in the precursor and the measured precursor diameter give an average density of ions N_i, which allows analysis of the pressure balance. The kinetic pressure of the plasma flow, arriving on the surface of the precursor, can be written as

$$P_{kin} = \frac{v}{2\pi RL} \cdot \frac{dm}{dt}. \tag{4}$$

https://doi.org/10.1017/S0263034601193122 Published online by Cambridge University Press

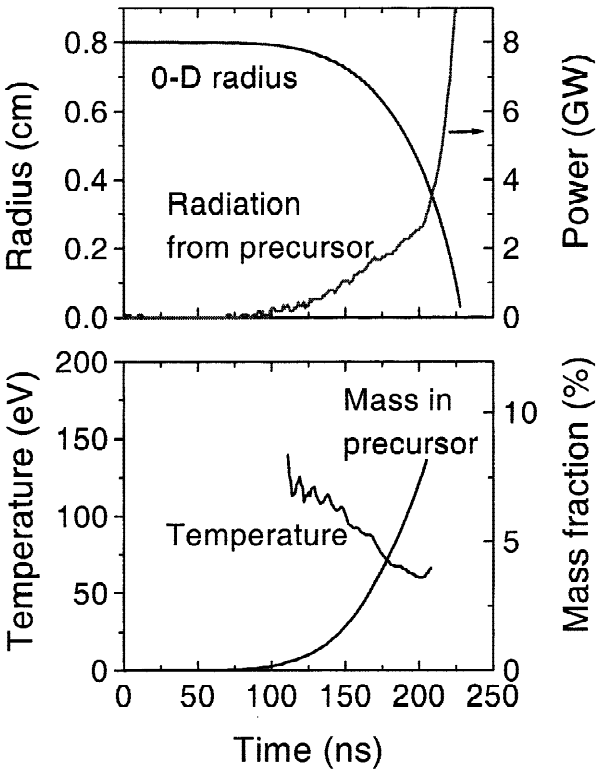

Fig. 16. Radiation power from Al precursor measured by open PCD detector (top) and the corresponding accumulated mass and temperature (bottom) of the precursor determined from the model of precursor formation.

This kinetic pressure is balanced by the thermal pressure in the precursor pinch:

$$P_{th} = (Z+1)N_i T. \tag{5}$$

Combination of Eqs. (3), (4), and (5) gives, for example, the temperature required for the equilibrium:

$$T = \frac{Q_{rad}}{\int Q_{rad}\,dt} \cdot \frac{m_i v R}{2(Z+1)}. \tag{6}$$

The precursor temperature calculated from Eq. (6) (shown in Fig. 16c) is in the range 50–100 eV, which is consistent with previously presented experimental data.

The condition of pressure balance [Eq. (6)] can be rewritten as a scaling for the equilibrium radius R of precursor with atomic number A:

$$R = \frac{\int Q_{rad}\,dt}{Q_{rad}} \cdot \frac{2(Z+1)T}{v m_i}. \tag{7}$$

Assuming that characteristic time-scales ($\sim \int Q_{rad}\,dt/Q_{rad}$) are the same for different materials, the expected ratio of equilibrium radii of precursor for W and Al arrays can be written as

$$\frac{R_W}{R_{Al}} \sim \frac{(Z_W+1)T_W}{(Z_{Al}+1)T_{Al}} \cdot \frac{A_{Al}}{A_W}. \tag{8}$$

For $T_W \sim T_{Al} \sim 50$ eV and Z corresponding to LTE ionization ($Z_W \sim 14$, $Z_{Al} \sim 7$), the above expression gives a ratio of $R_W/R_{Al} \sim \frac{1}{4}$, which is in surprisingly good agreement with experimental data (Fig. 14), which show that R_W/R_{Al} is $\sim \frac{1}{5}-\frac{1}{6}$.

The phenomenon of precursor formation in wire array z pinches could affect the generated X-ray pulse and is especially important for some applications which use a central target on the array axis, such as in dynamic hohlraum (Nash *et al.*, 1999) or static wall hohlraum (Olson *et al.*, 1999) concepts. For these applications, it is probably desirable to find conditions when the amount of the precursor plasma inside an array is minimal. At the same time, the precursor pinch on the array axis by itself has a number of interesting properties and can be used, for example, as a test-bed for radiation hydrodynamics and other basic plasma physics experiments. The dynamics of the precursor pinch, formed at stagnation of the converging plasma flow, strongly depend on the rate of cooling by radiation, which is expected to be optically thin for continuum radiation and optically thick for line radiation. In some conditions of precursor formation the transition from a collisionless to collisional regimes can also be studied. A high contrast in density between the precursor pinch and the plasma flow combined with the long lifetime of the pinch (~100 ns) make it feasible to design an experiment to study ionization balance. Another interesting possibility is to modify the wire array into a conical one, with different diameters of the top and bottom electrodes. Such a configuration produces a convergent conical plasma flow, which generates a highly supersonic, radiatively cooled plasma jet (Lebedev *et al.*, 2001).

5. INSTABILITIES IN THE CORONAL PLASMA AND IN THE CORES OF INDIVIDUAL WIRES OF A WIRE ARRAY

The early motion of the coronal plasma from the cores of wires towards the array axis changes the radial distribution of the mass in the array before the start of the implosion. In addition, and probably even more important, this process of gradual ablation of wire cores is not uniform along the wires. In this section we present experimental data on the development of instabilities in both the coronal plasma and wire cores.

Laser probing shows that the expansion of the coronal plasma from the wires occurs with the development of instabilities, which are seen from ~60 ns (~30% of implosion time) on schlieren and shadow images (Fig. 17). In contrast to single-wire z pinches (see, e.g., Kalantar & Hammer, 1993; Beg *et al.*, 1997; Ruiz-Camacho *et al.*, 1999), the

https://doi.org/10.1017/S0263034601193122 Published online by Cambridge University Press

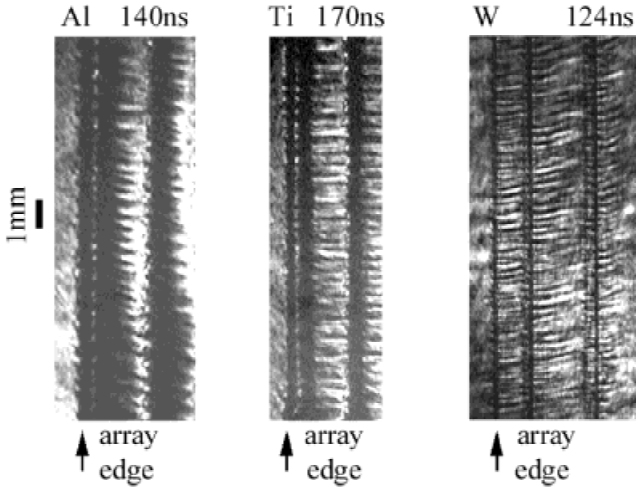

Fig. 17. Laser probing showing periodic structures in the coronal plasma for Al, Ti, and W wire arrays.

instability pattern around each wire is not axially symmetric. This is due to the $\mathbf{J} \times \mathbf{B}$ force of the global B_θ magnetic field of the array, sweeping the coronal plasma to the axis. Another significant difference from a single-wire *z* pinch is a quasi-periodic structure of the instability, seen in the streams of the coronal plasma from each wire. The wavelength (λ) of this structure ($\lambda \sim 0.5$ mm for Al) does not change with time from 60 ns (when first seen) to ~200 ns, when the wire cores start to move from their initial positions, and is roughly constant in all wires. However, as reported earlier (Lebedev *et al.*, 1998), there is no obvious correlation between the axial positions of the instability maxima and minima in different wires. The structure of the instabilities in the coronal plasma for other wire materials is similar to that observed for Al, but the wavelengths are different (~0.4 mm for Ti and ~0.25 mm for W). There is no change in wavelength of the instability for different interwire separations between 6.3 mm and 0.78 mm (for 8–64 wires) and for different initial wire diameters (15, 20, 25 μm for Al and 4, 5, 7.5 μm for W). It is interesting that a similar periodic instability structure was observed in linear wire arrays (Mosher *et al.*, 1998), with the same wavelength of ~0.25 mm for W wires.

The wavelength of the instability seen in the coronal plasma is comparable to the size of wire cores measured by X-ray radiography. Quantitative comparison can be performed by calculating the value of $ka = (2\pi/\lambda)a$, where λ is taken from the laser probing and the characteristic radius a is half of the core size (from radiography, see Fig. 4). The calculated ka (~1.6 and ~1.3 for Al and W, respectively) are almost the same. This implies that the size of the region (~core size), where formation and acceleration of the coronal plasma takes place, determines the development of the instability. The large extent of the instability structure in the inward radial direction ($\delta R \sim (5\text{–}10)\lambda$; Fig. 17) indicates a force-free character of these plasma streams inside the array. A constant (in time) wavelength suggests that the size of the region where the coronal plasma is generated does not change significantly, which is also in agreement with the radiographic data in the time interval of 140–200 ns.

The observed axial nonuniformity of formation and sweeping of the coronal plasma from the wires should leave an imprint on the axial mass distribution in the wire cores. This may act as a seed for the development of R-T instability during the acceleration of wires. Indeed, from ~80% of the implosion time, perturbations in wire cores start to be seen on the radiographic images. In Figure 18, obtained for an aluminum wire array, it is seen that the outer boundary of the wires (the array edge) is nonuniform with a characteristic spikes and bubbles structure, which indicates development of R-T instability in each individual wire of the array. The profiles of the film density along the wires (Fig. 18b) clearly show ~0.5-mm wavelength, the same as seen in the coronal plasma from early time. Wavelengths of instabilities mea-

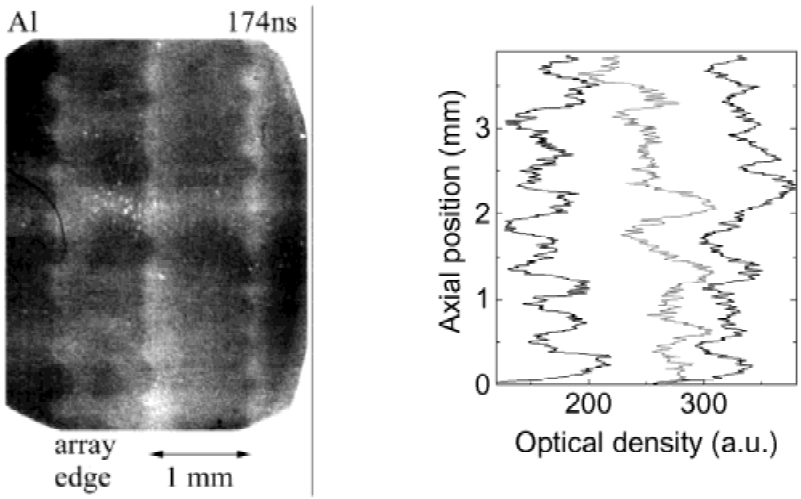

Fig. 18. Radiographic image showing instabilities in cores of Al wire array and corresponding axial profiles of film optical density (averaged radially over 0.2 mm).

https://doi.org/10.1017/S0263034601193122 Published online by Cambridge University Press

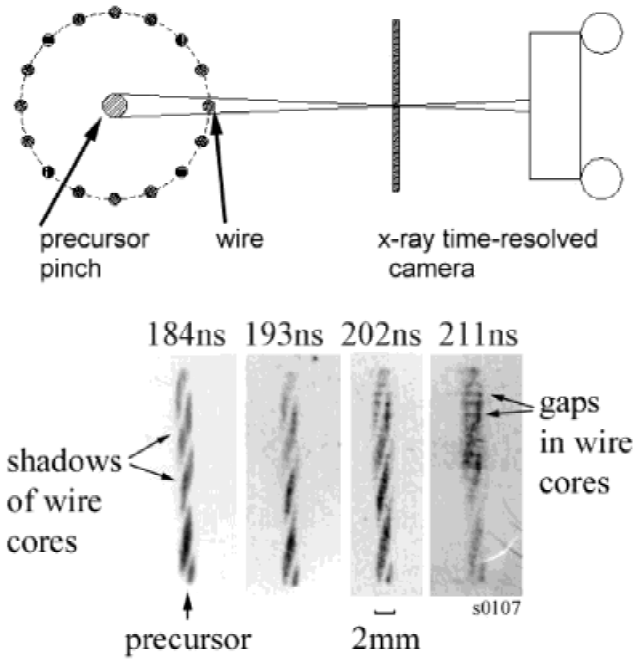

Fig. 19. Setup for X-ray radiography in z–θ plane using precursor emission (top). Gated soft X-ray images of the precursor obtained from the same shot, showing shadows of wire cores and formation of gaps in the cores at late time (bottom).

sured on the different wires in Figure 18 are the same, but the axial positions of spikes and bubbles in different wires generally do not coincide. These perturbations in individual wire cores act as a seed for the global $m = 0$ mode of R-T instability, which develops later during further acceleration of the array (Lebedev *et al.*, 1998). However, this global mode at this later time has a longer wavelength ($\lambda \sim 2$ mm). The mechanism, which determines the wavelength of the correlated global mode in this three-dimensional system, requires further study, but is probably related to the uncorrelated structure of perturbations in different wires. The $m = 0$ modes of the magneto-R-T instability have the fastest growth rates (Ryutov *et al.*, 2000), but the different random axial positions of spikes and bubbles in different wires prevent the development of a global $m = 0$ mode with the same wavelength as that seen in individual wires. For a longer wavelength mode, the effect of the perturbations being out of phase is smaller. Some indication of the preferential development of a longer wavelength structure (transition from 0.5 mm to ~2 mm) is seen in Figure 18, where the amplitude (contrast) of perturbations is larger if axial positions of perturbations in neighboring wires coincide. It should be emphasized that the measurements presented here were obtained for arrays with interwire gaps of ~1.5–3 mm. The question of whether correlation of inhomogeneities in wire cores will appear for smaller gaps requires further investigation, for example, by radiographic measurements of wire cores in positions close to the array center, where shadows of the neighboring wires are not overlapping, which was not possible in the present experimental setup (Fig. 3).

More data on the transition from the perturbations in the cores of individual wires to the global mode were obtained from X-ray radiography in the z–θ plane, using soft X-ray ($h\nu \sim 200$ eV) emission from the precursor on the array axis as a backlighter (Fig. 19). To simplify alignment of the diagnostic, the wire array (32 Al wires) was slightly twisted and shadows of four inclined wires are seen on each of the four images, obtained in the same shot. Formation of gaps (~100% mass modulation) with spatial separation of ~1.5–2 mm is seen on the last image at $t = 211$ ns. This separation is different from the $\lambda \sim 0.5$ mm of the imprinted perturbations, but coincides with the wavelength of the later global $m = 0$ mode of R-T instability (1.7–2.3 mm). Laser probing at late time also indicates transition to the longer wavelength structure. Figure 20a shows that the dominant wavelength of instability in each wire is the same 0.5 mm (Al), but formation of gaps at some axial positions is already seen.

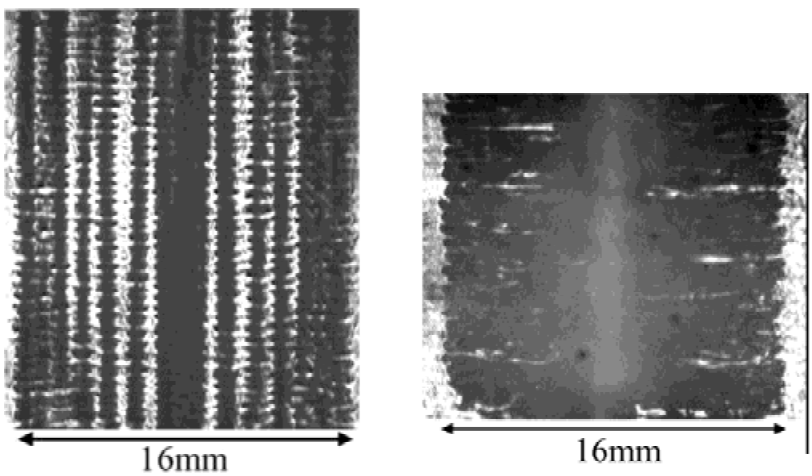

Fig. 20. Laser probing of wire array obtained in the same shot, showing uncorrelated instabilities in individual wires at $t = 180$ ns with dominant wavelength $\lambda \sim 0.5$ mm and later development of the global mode of the R-T instability ($t = 210$ ns).

https://doi.org/10.1017/S0263034601193122 Published online by Cambridge University Press

Data on the structure of the R-T instability later in time, when the global $m = 0$ mode of the instability is well developed, will be presented next.

6. FORMATION OF A GLOBAL MODE OF THE RAYLEIGH–TAYLOR INSTABILITY

Development of the global mode of the R-T instability is clearly seen on laser probing and gated soft X-ray images during the later stages of the array implosion, starting at time $t/t_{imp} \sim 0.7$–0.8. All these data show formation of ($m = 0$)-like structures with a characteristic wavelength of ~2 mm.

Gated soft X-ray images (filtered with 5-μm-thick polycarbonate, transmission window between 150 eV and 290 eV) start to show nonuniform emission from the wires and a number of bright spots are formed at the initial radial wire positions (Fig. 21a,b). These bright spots are formed on all wires and their axial positions are correlated between different wires. The axial spatial separation between the spots averaged over the length of the wire varies slightly with the number of wires in the array and is between 1.7 and 2.3 mm. The time of spot formation depends on the number of wires in the array, as shown in Table 1. The bright spots are formed in a time comparable with the interframe time (9 ns) of the camera (compare images in Fig. 21a) and emission from the bright spots lasts almost until stagnation time. During all this time the bright spots do not change their radial positions, which coincide with the initial positions of the wires.

Table 1. *Times of correlated bright spot formation (t_b) and their axial spacing (λ) in arrays with different number of wires. γ and G are the calculated growth rates and the number of e-foldings of the Rayleigh–Taylor instability.*

N	I_{max} (MA)	t_{imp} (ns)	t_b (ns)	λ (mm)	$\gamma(t_b)^{-1}$ (ns)	$G = \int \gamma\, dt(t_b)$
8	1.0	200	166	1.8	10.7	5.6
16	1.4	200	171	1.7	9.7	6
32	1.4	230	202	1.8	8.2	6.7
64	1.4	260	245	2.3	12.3	7.1

This behavior is consistent with the presence of a nonionized dense core in the wires, and formation of gaps in wire cores, which we discussed in the previous section.

It is instructive to find how time of formation of the global mode (time of appearance of the bright spots in X-ray images) scales with the number of wires in the array. For the classical RT instability, seeded perturbations will grow linearly as $\delta = \delta_0 \cdot \exp(G)$, where, $G \equiv \int_0^t \gamma(t)dt$, $\gamma = \sqrt{g \cdot 2\pi/\lambda}$, and g is the acceleration. A heuristic model by Haines (1998) suggests a scaling for the seeded level of radial perturbations, δ_0, with number of wires as $\delta_0 \propto N^{-1/2}$, due to averaging of the noncorrelated MHD instabilities which initially develop in individual wires. In this case, at the time when perturbations reach a fixed amplitude δ_*, the

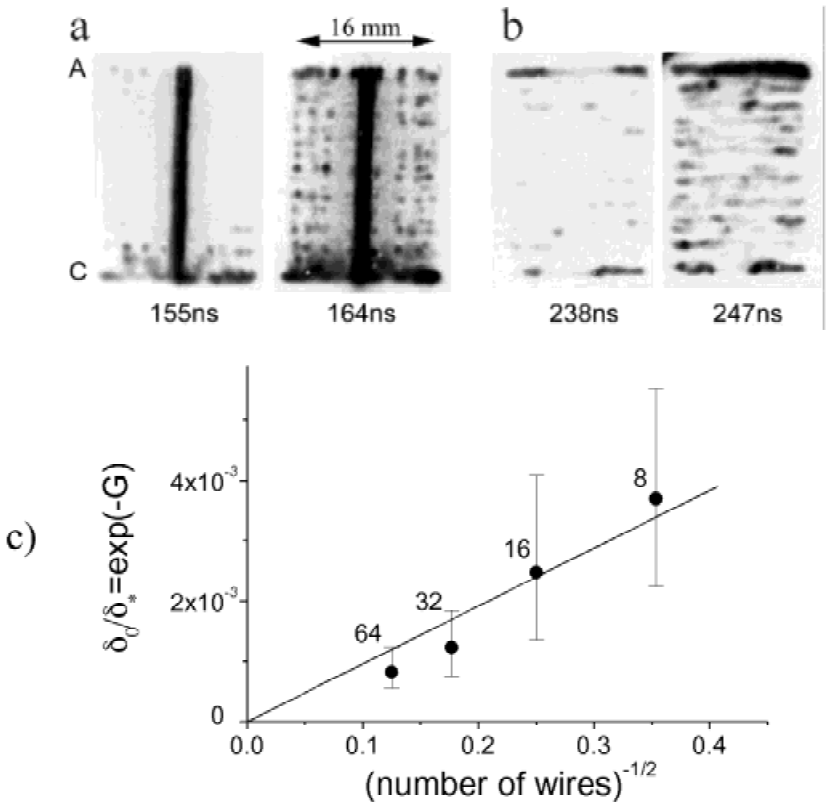

Fig. 21. Soft X-ray images showing formation of correlated bright spots due to the development of a global mode of R-T instability in arrays with 16 (a) and 64 (b) Al wires. Emission from the precursor observed on the axis of 16 wire array is not seen in 64 wire arrays after 200 ns. (c) Fit of the experimental data to the scaling law of Eq. (9).

https://doi.org/10.1017/S0263034601193122 Published online by Cambridge University Press

number of e-foldings, G, will be related to the number of wires, N, according to

$$\exp(-G) = \delta_0/\delta_* \propto N^{-1/2}. \quad (9)$$

For our experimental conditions the growth rate γ and the value of G at the time of the appearance of the bright spots in the X-ray images was calculated using the measured wavelengths of instability $\lambda = 1.7$–2.3 mm and taking acceleration g from 0-D calculations of the radius *versus* time. At the moment of bright spot observation, the calculated γ^{-1} of between 8.2 and 12.3 ns (see Table 1) for different numbers of wires agrees with the observed fast formation of the spots in about the interframe time of the X-ray camera (9 ns). The calculated value of G increases with the number of wires from 5.6 to 7.1 and the plot in Figure 21c shows that the experimental data agree reasonably well with the above scaling law.

Laser probing of the structure of the R-T instability at late time (Fig. 20b) shows the same characteristic wavelength of $\sim$2 mm, with the R-T bubbles reaching the axis of the array, while the spikes are anchored to the initial array radius, due to the existence of the dense cores. It is interesting to find out if the structure of the global mode of R-T instability will be different in twisted wire arrays. The growth of the instability can be different in this configuration due to the hourglass shape (Douglas *et al.*, 1997*a*; Golub *et al.*, 1999) of the envelope of twisted wire arrays. In addition, the generation of axial magnetic field B_z could be expected inside twisted wire arrays, if the current flow follow the wires.

Figure 22a shows results of laser probing of a 32 Al wire array, twisted at an angle of $3\pi/8$, where the formation of a global ($m = 0$)-like mode is clearly seen. The spikes of instability are again anchored to the initial wire positions, in the same way as in cylindrical arrays, and thus the initial hourglass shape of the twisted array is seen. The wavelength of the global mode is the same as in cylindrical arrays. However, directions in which bubbles of the R-T instability grow are different for different axial positions along the array. In each axial position the growth of the bubble occurs in the local direction of $\mathbf{J} \times \mathbf{B}$ force, perpendicular to the "envelope" of the array. This indicates that the current has a radial component and flows in the vicinity of the wires, not through the coronal plasma inside the array in the z-direction. Measurements by magnetic probes of the axial magnetic field inside the array show that B_z up to ~ 2 T (at $t \sim 200$ ns) is generated in this configuration, which is about 10% of the azimuthal magnetic field at this time. The magnitude of the B_z, smaller than the expected $\sim$25% of B_φ for the used angle of array twist ($3\pi/8$), could be explained by the skin effect in the electrodes. The generation of the axial magnetic field in the twisted wire array indicates that a significant fraction of the current is concentrated in the vicinity of the cores, at a distance less than interwire separation ($\sim$1.5 mm in this experiment).

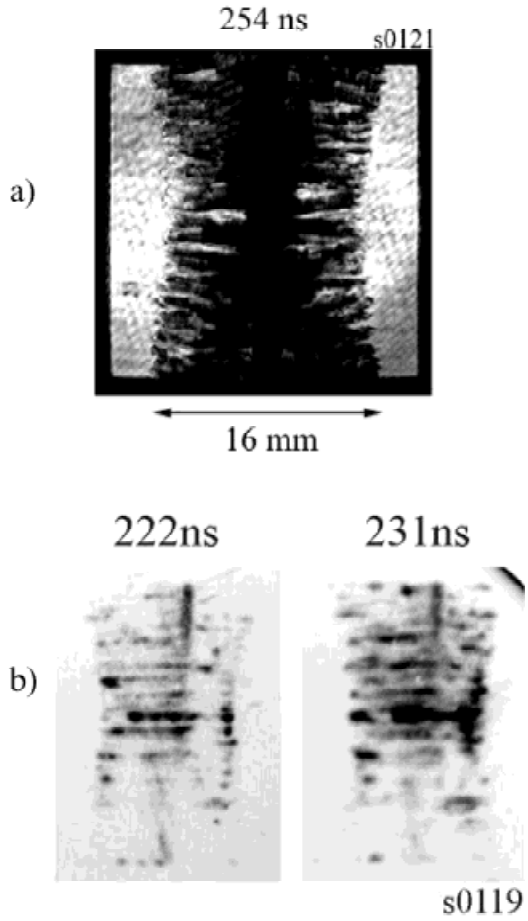

Fig. 22. Laser probing (a) and soft X-ray images (b) of the development of the R-T instability in twisted wire arrays.

The gated soft X-ray images of twisted arrays also show formation of the global $m = 0$ mode of instability (Fig. 22b). It is seen that bright spots appear first in the central part of the array, where the $\mathbf{J} \times \mathbf{B}$ force accelerating the plasma has its maximum, and in about 10 ns the $m = 0$ mode develops along the full length of the array. This difference in the starting time of the global mode is also in agreement with the different amplitude of the bubbles seen in different axial positions by the laser probing (Fig. 22). This zippering of the implosion, from the array center to the ends, resulted in a longer X-ray pulse generated at stagnation of the twisted arrays in our experiments. However, for larger initial array radii the effect of zippering could be less significant.

7. IMPLOSION DYNAMICS OF Al AND W WIRE ARRAYS

7.1. Experimental data

The implosion dynamics of wire cores were measured by radial optical streak photography. It is instructive to compare these data (Fig. 23) with a 0-D implosion model, which

https://doi.org/10.1017/S0263034601193122 Published online by Cambridge University Press

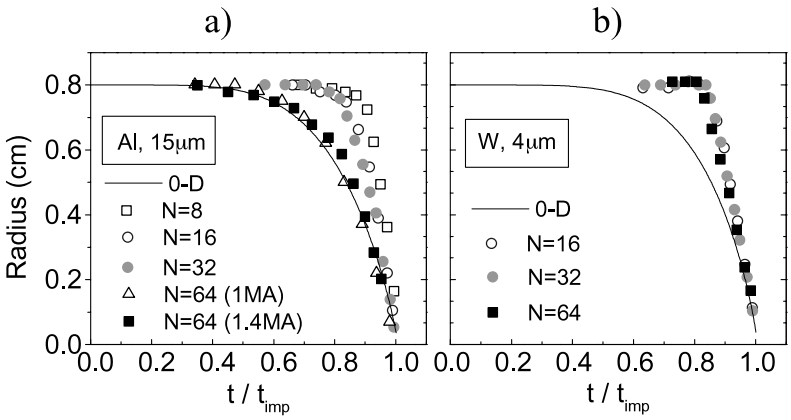

Fig. 23. Implosion trajectories measured from optical streaks for 8, 16, 32, and 64 Al (15 μm) wire arrays (a), and for 16, 32, and 64 W (4 μm) wire arrays (b). Time is normalized on the implosion time.

assumes that the array implodes as a hollow plasma cylinder accelerated by the global $\mathbf{J} \times \mathbf{B}$ force. The stagnation times measured from optical streaks and X-ray signals for arrays with different wire number agree to within <5% with the times predicted by the 0-D model, as routinely observed in wire array *z*-pinch implosions (see, e.g., Sanford *et al.*, 1998; Spielman *et al.*, 1998). However, the implosion trajectories for small wire number arrays deviate significantly from that predicted by the 0-D model. For 8, 16, and 32 Al wire arrays the cores remain in their initial positions until about 80% of the implosion time (Fig. 23). This time coincides with the time when the imprint of instabilities on wire cores is detected by radiography. The stationary position of the wires can only be understood if no force is applied to the wire cores until this time, that is, the current up to this time flows mainly in the low-density coronal plasma immediately around the cores, providing ablation of the cores and acceleration of the coronal plasma towards the array axis. The sudden acceleration of the cores would then occur at the time of current transfer to the cores. For arrays with different wire numbers, the current per wire at the time when the wires start to move varies by a factor of ~7 (Table 2), and is definitely not a primary parameter here. The relative times of acceleration ($t_{ac}/t_{imp} \sim 0.8$), however, are the same for 8, 16, and 32 Al wire arrays and for 16, 32, and 64 tungsten wire arrays (Fig. 23), despite a very large difference in the thermal and ionization properties of Al and W. Assuming that all the current is transferred to the wire cores at the moment of ~70–80% of implosion time, a mass fraction of ~25% remaining in the cores would provide the observed fast implosion.

Table 2. *Times of the wires' acceleration (t_{ac}) and corresponding current (I_{ac}: total, I_{ac}/N: per wire) for arrays with different wire number. t_{imp} is the implosion time of the array.*

N	I_{max} (MA)	t_{imp} (ns)	t_{ac} (ns)	t_{ac}/t_{imp}	I_{ac} (MA)	I_{ac}/N (kA/wire)
8 Al	1	200	168	0.84	0.76	95
16 Al	1	230	180	0.79	0.82	51
32 Al	1	270	208	0.77	0.95	30
64 Al	1	320	175	0.54	0.79	12
64 Al	1.4	270	145	0.53	0.85	13
16 W	1	200	165	0.83	0.75	47
32 W	1	230	190	0.83	0.87	27
64 W	1	270	220	0.82	0.97	15

A qualitative change in the implosion dynamics was observed in Al arrays when the wire number increases from 32 to 64 (the interwire gap decreasing from 1.57 mm to 0.78 mm). The measured array radius (Fig. 23a) for 64 wires follows the 0-D trajectory very closely, and the inward displacement of wires from their initial radius occurs earlier (even in absolute time) than for a 32 wire array, despite a smaller (by a factor of 2) current per wire. The decrease of the interwire separation also changes the inward streaming of the coronal plasma at late time. This is evident from an early decay of the precursor emission, which is generated by stagnation of the coronal plasma streams on the array axis. The decay of precursor emission is seen on optical streaks, soft X-ray images (see Fig. 21b) and PCD signals, and for 64 wire arrays the precursor emission is not seen after about 200 ns, while for 32 and smaller wire number arrays, the emission lasts until stagnation. This gives, taking into account the delay in the arrival of the plasma on the axis (~60 ns), the time of the effective plasma merger of ~140 ns. It is interesting to note that the gap at which transition to 0-D implosion trajectory occurred for 64 Al wire arrays in our experiments is essentially the same as the critical gap identified in experiments with Al arrays on the 7-MA Saturn facility at SNL (Fig. 4 in Sanford *et al.*, 1996).

The observed qualitative change in the implosion dynamics for Al wire arrays occurred when the ratio between interwire separation (0.78 mm) and the characteristic size of wire core (0.25 mm) became equal to about 3. This could be related to the fact that when the ratio of the interwire separation to the wire diameter equals π, the contribution of the "private" magnetic flux of each wire to the array inductance (Katzenstein, 1981) is zero, and the array inductance be-

https://doi.org/10.1017/S0263034601193122 Published online by Cambridge University Press

comes equal to the inductance of a thin shell. This may affect the radial distribution of current around wire cores, in analogy to the inductive current division in nested wire arrays, where the current fraction in the inner array is proportional to the difference between the array inductance and the mutual inductance [the latter equal to inductance of a shell with radius equal to array radius (A.L. Velikovich, pers. comm.)].

For tungsten wire arrays, which have a core size a factor of ~2.5 smaller, the transition to a 0-D implosion trajectory for 64 tungsten wire array was not observed (Fig. 23b), and, unlike for aluminum, emission from the precursor continued until stagnation. This implies the absence of effective merger of plasmas from adjacent wires and instead a continuous injection of material from wire cores. Assuming that for merger to take place the same ratio of the gap to the size of wire core is necessary for both Al and W, a gap of <0.3 mm would be required to see this transition in tungsten wire arrays.

7.2. Ablation rate of wire cores and seeding of perturbations in low wire number arrays

To describe the dynamics of core–corona plasma in wire arrays, a fully 3-D MHD model with a "cold start" is required (e.g., of a type discussed by Chittenden *et al.*, 2001), which is not available at present. Here we will present a simple phenomenological analysis, which provides an estimate of the ablation rate of the wire (and corresponding radial mass distribution) and an estimate of the maximum level of perturbations in wire cores due to ablation.

The experimental data presented in this article show that for sufficiently large interwire gaps, the wire cores are stationary until ~80% of the implosion time. This is only possible if a $\mathbf{J} \times \mathbf{B}$ force is not applied to the cores; instead only some fraction of the mass is continuously ablated from the cores and accelerated towards the array axis. We will assume that during all this time the current is flowing in some small region close to the wire cores, and also that the velocity V of the coronal plasma is constant after leaving this current-carrying region (Fig. 24a). The assumption of constancy in time velocity is consistent with that observed in the experiments constant in time "hardness" of the X-ray emission from the precursor and with results of MHD simulations of wire arrays (Chittenden *et al.*, 1999). The ablation rate required to support this quasi-stationary configuration can be found from the equation of motion, written as follows:

$$V\frac{dm}{dt} = -\frac{\mu_0 I^2}{4\pi R_0}. \tag{10}$$

The right-hand side in this equation is similar to that used in the 0-D model of z-pinch implosions (see, e.g., Ryutov *et al.*, 2000), the only difference being that the radius R_0 in Eq. (10) is constant in time (stationary wire cores). If velocity of the plasma V is known, the mass (δm) ablated from the wires until some moment t can be found as

$$\delta m(t) = \frac{\mu_0}{4\pi V R_0}\int_0^t I^2 dt. \tag{11}$$

For our experiments with Al arrays, the velocity of the coronal plasma is 1.5×10^7 cm/s (measured by end-on laser probing), which allows us to calculate the ablated mass, as shown in Figure 24. The ablated mass calculated from this model is in good agreement with the experimental estimate of the mass accumulated in the precursor (see Sect. 4), and with results of 2-D (x–y plane) MHD computer simulations, described in Chittenden *et al.* (1999, 2001). It is seen from Figure 24 that the ablation fraction is about 5% at 50% of the implosion time, and reaches the ~30–40% level at 70–80% of the implosion time, when the cores start to move.

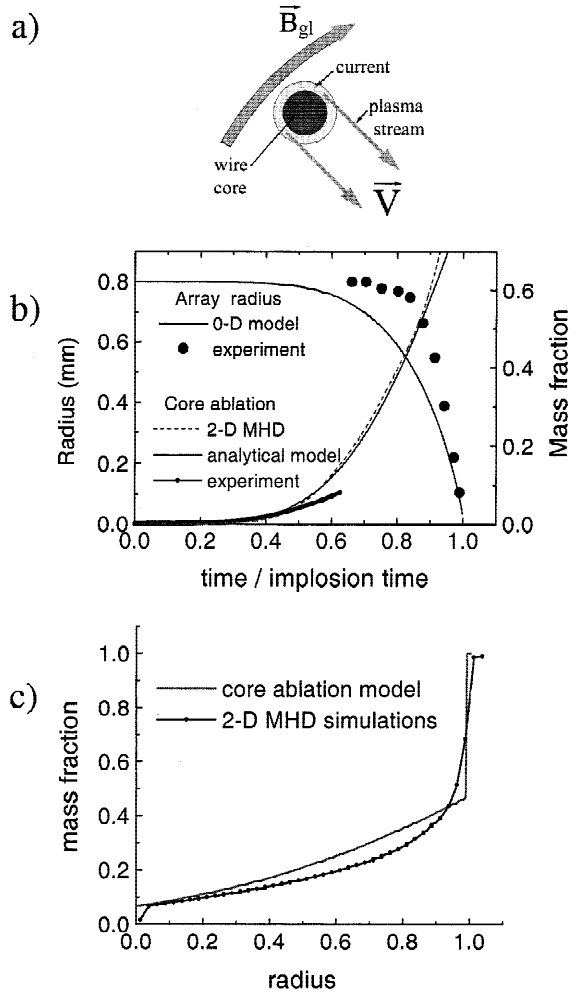

Fig. 24. Model core ablation in wire array with stationary cores (a) and comparison (b) of the ablated mass fraction calculated from this model [Eq. (11)] with 2-D (x–y plane) MHD simulations and the experimental estimate found from the precursor radiation [Eq. (3)]. Radial profile of mass integral (c) at 80% of the implosion time calculated from the ablation model and obtained from the 2-D MHD simulations.

https://doi.org/10.1017/S0263034601193122 Published online by Cambridge University Press

This model of the ablation rate can be used to estimate a maximum (for a particular moment of time) level of mass perturbation in wire cores. Indeed, as was discussed in Section 5, the ablation of the cores occurs nonuniformly along each wire, with the characteristic spatial scale of the nonuniformity being comparable to the size of the cores. The maximum possible level of mass modulation in each wire core (due to nonuniform ablation) is equal to the ablated mass fraction. For example, at 50% of the implosion time, about 5% of the mass was ablated from the wires, which gives a maximum level of mass modulation in each wire of ~5%. As this mechanism of seeding of perturbations works for large interwire gaps, it is reasonable to assume that perturbations in each wire are not correlated. The level of perturbations, averaged over number of wires N, will be a factor of $N^{1/2}$ smaller, as discussed in the Heuristic model by Haines (1998). As the spatial scale of perturbations in each wire is known (determined by the core size; see Sect. 5), the spectrum of perturbations averaged over N wires in the array can be also found.

For arrays with interwire separation less than some critical gap, the streaming of the coronal plasma (and core ablation) stops earlier as the number of wires increases. As a result, the fraction of mass ablated up to this moment decreases with the increase of wire number, which will give a faster decrease of the perturbation level with wire number than the $N^{-1/2}$ scaling law. This could be responsible for the faster rise of X-ray power for number of wires above some critical number, as observed in experiments (Sanford *et al.*, 1996) on the Saturn generator, but more study is needed here.

This simple model of core ablation and seeding of perturbations in a wire array can be made more quantitative, and will be discussed in more detail elsewhere. It would be interesting to use the perturbations determined in this way (say at $t = 80\%$ of the implosion time) and the radial distribution of mass at this moment (Fig. 24c), as the initial conditions for 2-D (r–z plane) MHD codes, instead of the random (cell to cell) density perturbations presently employed. The small size of wire cores for tungsten found in our experiments indicates that this approach can be justified for W wire arrays even with large wire number (~200 at 4-cm diameter). To estimate from this model the level of perturbations and the radial mass distribution in wire arrays imploded by a current larger than in the present experiments, measurements of the radial inward velocity of the coronal plasma are required. However, it is interesting to note that the same dimensionless time (~80%) of the beginning of the movement of the cores was recently observed for W wire arrays imploded by a ~3 MA current (in ~100 ns) in experiments on the ANGARA-V facility (V.P. Smirnov *et al.*, pers. comm.). This suggests that the mass fraction ablated from the cores until this moment was again ~50%, as in our experiments, and could partially justify the use of the mass distribution shown in Figure 24c as a starting point for 2-D (r–z plane) MHD simulations.

8. DIFFERENT DYNAMICS MODES OF NESTED WIRE ARRAYS

For further improvement of the implosion quality in z pinches, it was proposed to mitigate R-T instabilities by the use of an additional mass inside the imploding plasma (Goldberg & Velikovich, 1993; Hammer *et al.*, 1996). Realization of this approach by the use of nested wire arrays resulted in a 40% increase in the radiated power and 280-W, 1.8-MJ, 4-ns pulses of soft X-ray radiation (Deeney *et al.*, 1998). However, there is only limited understanding of the performance of nested wire array z-pinch loads. Two-dimensional magnetohydrodynamic modeling (in the r–z plane; Douglas *et al.*, 1997*b*; Peterson *et al.*, 1999) shows a decrease of the R-T amplitude when the arrays collide and can reproduce the increase in the main radiation pulse, but requires the assumption that both wire arrays have been converted into azimuthally uniform plasma shells before they collide. The thickness of the shells is a free parameter in this model, collision of the shells is assumed to be inelastic with conservation of momentum, and the excess of the kinetic energy is radiated at the strike. The experimentally observed radiation when the arrays collide (Deeney *et al.*, 1998) is much smaller than predicted by the model, which could be due to three-dimensional effects such as arrays being composed of expanded but still discrete wires, which cannot be included in 2-D (r–z) modeling. Davis *et al.* (1997) have considered the implosion dynamics of nested arrays in the r–θ plane using a model of discrete wires with the current being inductively distributed between the arrays, and have discussed the possibility of penetration by the outer array through the gaps in the inner array, with fast inductive switching of the current to the inner array at the time of strike. The analysis of nested wire array experiments on the Z facility at SNL using this model was reported by Terry *et al.* (1999).

Here we describe experiments which were designed to study implosion dynamics of nested wire arrays in conditions where the implosion phase before the final stagnation can be diagnosed. In these experiments, the nested wire array was composed of a 16-mm-diameter outer array and 8-mm-diameter inner array. Both arrays consisted of 16 aluminum wires of 15-μm diameter. The length of the outer array was 2.3 cm. Figure 25 shows two different modes of connection of the inner array to the electrodes. In the first case (Fig. 25a) the length of the inner array was the same as the outer array and the expected current in the inner array, calculated from numerical solution of the magnetic field diffusion equation in the r–θ plane (as in Chittenden *et al.*, 1999), was ~20% of the total current. In the second configuration (Fig. 25b), the inductance of the inner array was deliberately increased by use of a longer (additional 3 cm at each end) inner array. As a result, only a short burst of current (~8 kA) through the inner array was measured by the B-dot probe (shown in Fig. 25b) in the first ~20 ns, coincident with the time of higher resistivity of the outer array wires undergoing phase transitions. The high imped-

https://doi.org/10.1017/S0263034601193122 Published online by Cambridge University Press

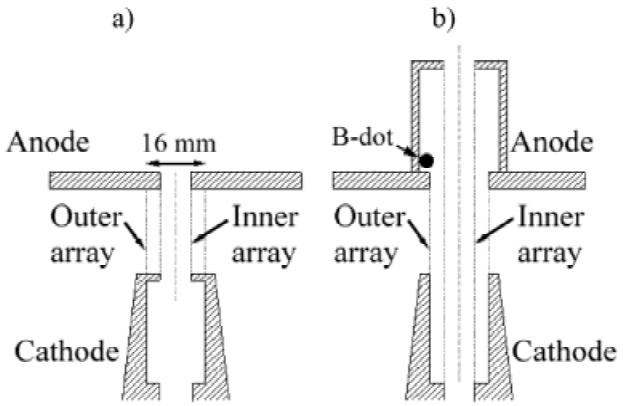

Fig. 25. Schematic of nested wire arrays with low inductance (a) and high inductance (b) connection of the inner array.

ance of the generator meant that the measured total current through the load was the same for both configurations of the nested arrays and for the single array.

Figure 26 shows side-on shadowgrams obtained for the two configurations. For the low inductance connection (low L), from early time, the current in the inner array is high enough to provide similar expansion of the wires in both the inner and outer arrays (Fig. 26a). For the high inductance case (high L), there is no measurable expansion of the wires in the inner array at 72 ns, and only a very small expansion of $<$0.1 mm was measured at 132 ns, in contrast to the $\sim$0.6-mm diameter measured for the wires of the outer array (Fig. 26b).

The set of radial optical streak photographs in Figure 27 shows the implosion dynamics in the two configurations. For the high-L case, emission from the inner array starts much later than for the low-L connection, is less intense, and is probably due to interaction with the flux of coronal plasma

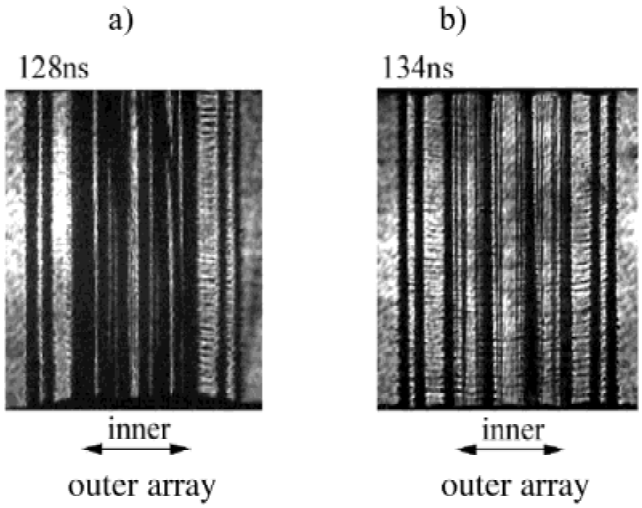

Fig. 26. Side-on laser shadowgrams showing the difference in wire expansion of the inner and outer arrays for the low L (a) and high L (b) arrays.

from the outer array accelerated by the global magnetic field. The existence of the coronal plasma flow is evident from the formation of the precursor pinch on the array axis. Figure 27 shows precursor formation in both configurations at $\sim$135 ns (roughly the same time as for single arrays) with precursor emission observable until $\sim$220 ns. Gated soft X-ray images (Fig. 28a) also show precursor pinches similar to those observed in single arrays, and emission from the wires of the inner array only. As with single arrays (Lebedev *et al.*, 1999), current flowing in the outer array does not produce observable X-ray emission, which confirms that the emission observed from the inner array is due to collision of the coronal plasma from the outer array with the inner array wires. In both cases, end-on laser probing of the inner wire array at $\sim$120 ns (just before the time of the precursor pinch formation) shows the interior of the inner array filled with plasma but with the laser beam still able to propagate along the array axis (Lebedev *et al.*, 2000*a*). All these measurements indicate that the inner array is, in both configurations, transparent to the incoming flux of the coronal plasma from the outer array.

Implosion of the main mass of the array occurs much later in the discharge than the formation of the precursor pinch. The apparent motion of wires in the outer array of both nested configurations starts at 200–210 ns (Fig. 27), and the deviation of the implosion trajectory from the 0-D is the same as was discussed earlier for single wire arrays (Sect. 7). As a result of the observed delay in acceleration of the wires, the outer array reaches the initial position of the inner array later than the 205 ns predicted by a 0-D model, but the measured velocity of the plasma at this time ($\sim$23 cm/μs) is twice the predicted 0-D velocity. The measured time of $\sim$225 ns, when the outer array reaches the initial position of the inner array was the same for both nested configurations. The implosion dynamics however were completely different.

For the high-L configuration, the inner array does not move from its initial radius before the strike, and the measured velocity, immediately after the strike, is zero. This implies that no momentum was transferred to the inner array and the plasma of the outer array has passed through the inner array without interaction. This is radically different from the model of colliding plasma shells, where, due to conservation of momentum, the velocity of the ensemble after the strike would be half of the velocity of the outer array just prior to impact. The measured implosion trajectory of the inner array is in excellent agreement with the 0-D model (Fig. 27c), assuming that from 225 ns onwards all the current is flowing through the inner array (the central, 2.3-cm-long part of it and through the radial plasmas left by the imploded outer array).

Very different implosion dynamics are observed for nested arrays with low-L connections to the inner array. The radial position of the outer array (Fig. 27d) after $\sim$220 ns follows quite closely a 0-D trajectory with 78% of the current in the outer array (fraction calculated from numerical solution of the magnetic field diffusion equation in the r–θ plane, as in

https://doi.org/10.1017/S0263034601193122 Published online by Cambridge University Press

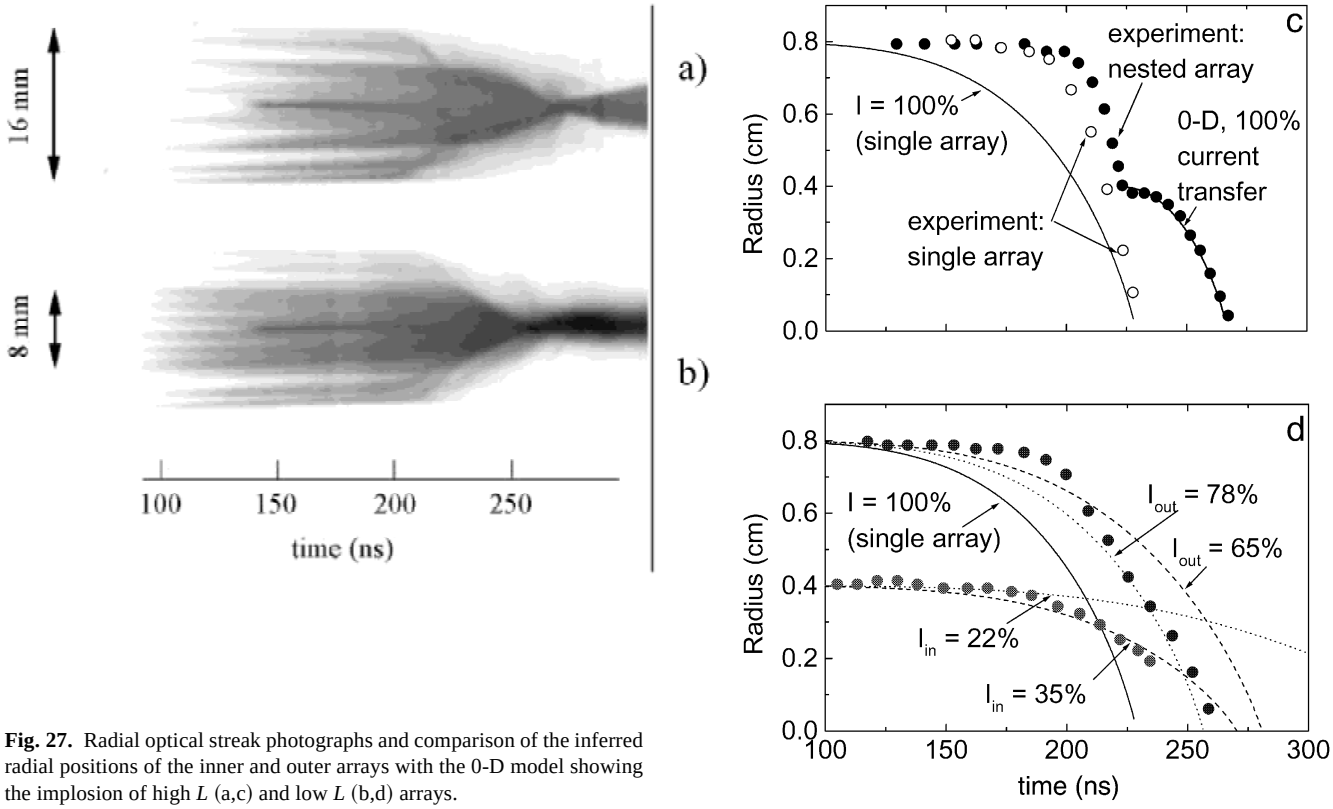

Fig. 27. Radial optical streak photographs and comparison of the inferred radial positions of the inner and outer arrays with the 0-D model showing the implosion of high L (a,c) and low L (b,d) arrays.

Chittenden *et al.*, 1999). The inner array starts to move at ~175 ns and initially follows the 0-D trajectory for the remaining 22% of current, but later, from ~200 ns, the inner array implodes faster and the closest 0-D trajectory corresponds to ~35% of the current. As a result, the two arrays apparently stagnate simultaneously and no collision of the arrays is observed. Two-dimensional MHD simulations in the r–θ plane (Chittenden *et al.*, 2001) indicate that the trajectory of the inner array in this case is the result of trapping of magnetic flux between the arrays which acts as a buffer zone, preventing collision of the arrays during implosion. The transfer of momentum to the inner array from the inward flow of the coronal plasma is also significant.

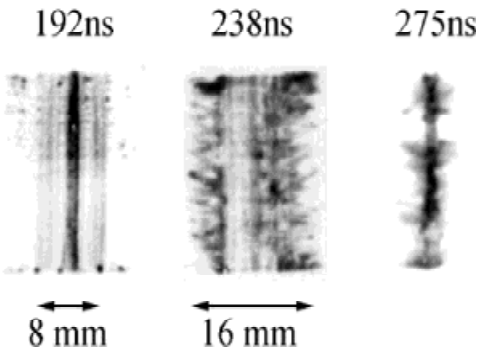

Fig. 28. Soft X-ray images of nested arrays (high L case) showing uniform emission from the inner array and the start of bright spot formation in the outer array (t = 192 ns), the structure of the R-T instability (t = 238 ns), and final stagnation (t = 275 ns).

The time history of soft X-ray emission recorded by a PCD detector with a 5-μm-thick polycarbonate filter (transmission window 180–290 eV) is shown in Figure 29. In all cases the main X-ray pulse starts at the time of stagnation, measured from the streak images. For a single array, the pulse rise time (10–90%) is 40 ns. Nested wire arrays (in both configurations) produce X-ray pulses with much shorter rise times of 10–13 ns, despite the long implosion times (260–270 ns) and small numbers of wires. The mechanism of X-ray pulse shortening is probably different for the two configurations. For the low-L case, the magnetic field between the arrays could affect the growth of the R-T instability, but more data are needed here. In the high-L case, almost the maximum current is rapidly applied to the inner array and the R-T instabilities in the inner array have less time to grow (smaller $\int \gamma\, dt$) due to a short implosion time. Figure 29b shows the X-ray signal from a nested array with high inductance connection; the times of precursor formation, array collision and stagnation, measured from the streak image are indicated. It is interesting to note that the shape of the X-ray pulse is very similar to that observed in nested array implosions on Z (see Fig. 2 in Deeney *et al.*, 1998), despite a very large difference in the number of wires in the arrays (240 in outer and 120 in inner in Deeney *et al.*, 1998, and 16/16 in our experiments). The differences in the interwire gaps, and so forth, however, mean that we cannot

https://doi.org/10.1017/S0263034601193122 Published online by Cambridge University Press

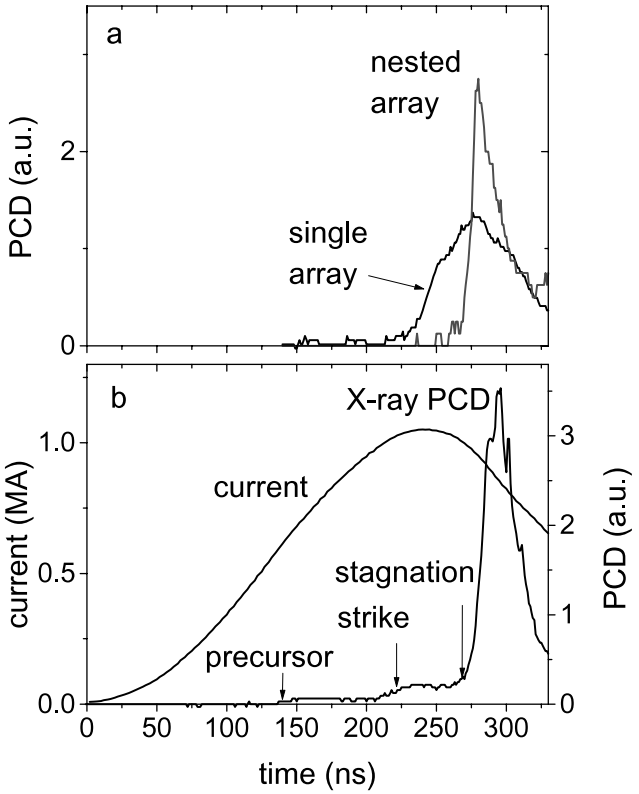

Fig. 29. (a) Soft X-ray signals from a single wire array and a nested array with a low L inner, and (b) from a nested array with a high L inner and the total current waveform.

conclude from this comparison that this mode is in operation on Z.

Gated soft X-ray images show that at the time of the radiation peak (270–290 ns) the pinch diameter in both nested array configurations is ∼1.5 mm (Fig. 28). During the run-in phase, the development of R-T instabilities leads to the formation of axially correlated bright spots at ∼195 ns on the wires of the outer array (as in single arrays; Lebedev *et al.*, 1998, 1999). Later in time, instability structure with a characteristic axial wavelength of ∼2 mm is clearly seen between the initial radii of the outer and inner arrays. The spikes of the R-T are anchored to the initial diameter of the outer array, which could be explained by the presence of un-ionized dense wire cores.

9. CONCLUSIONS

Present experiments show that the implosion dynamics of wire arrays strongly depend on the core–corona structure of the plasma formed from the individual wires of the array. The dense cores of wires survive for a substantial part of the implosion, and for arrays with interwire separation above some critical value, the cores remain in the initial positions of wires until ∼80% of the implosion time. In this case, the current flowing just around the wires provides continuous ablation of the cores and acceleration of the coronal plasma to the array axis. In contrast to the situation where all wire mass stays intact and the $\mathbf{J} \times \mathbf{B}$ force delivers momentum to all the mass (in the form of either shell or discrete wires), in the system with a heterogeneous structure of the plasma, the same momentum is delivered to a small fraction of the mass. It appears that for large interwire gaps, this situation is supported self-consistently until ∼80% of the implosion time, when about half of the mass is ablated and the ablation rate is no longer capable of providing the mass flux required for momentum balance. From this moment the remaining mass implodes rapidly and the final implosion time agrees with that expected from the 0-D model, though the implosion trajectory is significantly different from the 0-D one.

It was found that for Al wire arrays, the decrease of the interwire separation to 0.8 mm resulted in a qualitative change in the implosion dynamics. The implosion trajectory started to follow the 0-D trajectory, and the inward streaming of the coronal plasma from the cores stopped before the wires started to move (at ∼50% of t_{imp}). This critical interwire gap is related to the size of dense wire cores, measured in our experiment by X-ray radiography. For Al wire arrays, the transition to 0-D-like implosion occurred when the ratio between the gap and the core size became equal to ∼3. The identified critical gap for Al wire arrays in our experiments is essentially the same as was observed in experiments with Al arrays on 7-MA Saturn facility at SNL (Fig. 4 in Sanford *et al.*, 1996). For tungsten, the core size is significantly smaller (∼0.1 mm instead of ∼0.25 mm for Al), which would require an interwire separation of ∼0.3 mm to see a similar transition in tungsten wire arrays. This explains the absence of transition to a 0-D implosion trajectory in our experiments, and suggests that similar deviation of the implosion from a shell-like one probably occurs in tungsten wire array experiments at SNL even for large wire number arrays.

The formation of the core–corona plasma structure in wire arrays and the early acceleration of the coronal plasma towards the array axis play a significant role in the seeding of axial mass perturbations in wire cores, thus providing the initial conditions for the growth of the Rayleigh–Taylor instability. The streams of the coronal plasma are found to be nonuniform in the axial direction. The wavelength of this nonuniformity is determined by the size of wire cores, and the measured value of ka is ∼1.5 ($\lambda = 0.5$ mm for Al and 0.25 mm for W). The corresponding axial nonuniformity of ablation provides perturbation of mass distribution in the cores. The first step in the R-T development is seen as an imprint of perturbations on the wire cores at the time of the array acceleration. The wavelength of this imprinted structure measured by X-ray radiography is the same as was seen in the coronal plasma from early time. Further acceleration of the array leads to very fast formation of a global $m = 0$ mode at a longer wavelength of ∼2 mm. For large interwire separations the perturbations in different wires are uncorrelated, and the amplitude of perturbations for the global mode (found by averaging over the azimuth) scales with the num-

https://doi.org/10.1017/S0263034601193122 Published online by Cambridge University Press

ber of wires in the array as $N^{-1/2}$ (Haines, 1998), which is supported by our experimental data. For smaller interwire gaps, the early decrease of the mass ejection from the cores should decrease the level of perturbations produced by the nonuniformity of the ablation. As a result, the seed level of perturbations in wire cores should become significantly smaller. This effect could be responsible for the faster decrease of the seed level in comparison with the $N^{-1/2}$ scaling provided by an averaging of the perturbations over the larger number of wires. This could explain the sharp rise of the X-ray power with wire number for the gaps below critical, observed in Al wire array experiments (Sanford *et al.*, 1996) at SNL, though we cannot exclude other possible explanations. A significantly smaller size of wire cores for tungsten may mean that a similar transition (critical gap) was not reached for W arrays even with the highest wire numbers.

The experiments with nested wire arrays show that significant sharpening of the X-ray pulse can be obtained in different modes of interaction between the outer and inner arrays, and even for arrays with small wire numbers. For the mode with a transparent inner wire array, the outer array passes through the inner, which then implodes due to the fast transfer of current from the outer array at this time, as was theoretically predicted by Davis *et al.* (1997). The almost maximum current is rapidly applied to the inner array in this case, and the R-T instability has much less time to grow. In addition, it is possible that the level of perturbations in the inner array, which initially does not carry current, is smaller in this mode. It would be interesting to test the operation of nested wire arrays with a transparent inner at a current larger than the 1-MA level in present experiments.

ACKNOWLEDGMENTS

The authors gratefully acknowledge many interesting discussions on the physics of wire array *z* pinches with scientists of Sandia National Laboratories, in particular Drs. Keith Matzen, Chris Deeney, Rick Spielman, and Tom Sanford. We also would like to thank Drs. Jack Davis, Sasha Velikovich, and Bob Terry of the Naval Research Laboratory for discussions on physics of nested wire arrays and *z*-pinch plasma radiation sources. We are very grateful to Prof. David Hammer of Cornell University for the numerous discussions and especially for the help in implementing of X-ray radiography diagnostic. This work was supported by Sandia National Laboratories (contract BF6405) and the Department of Energy (contract CFDA91.112).

REFERENCES

Aivazov, I.K. *et al.* (1988). *Sov. J. Plasma Phys.* **14**, 110.
Beg, F.N. *et al.* (1997). *Plasma Phys. Controlled Fusion* **39**, 1.
Chittenden, J.P. *et al.* (1999). *Phys. Rev. Lett.* **83**, 100.
Chittenden, J.P. *et al.* (2000). *Phys. Rev. E* **61**, 4370.
Chittenden, J.P. *et al.* (2001). *Laser Part. Beams* **19**, 323 (this issue).
Davis, J. *et al.* (1997). *Appl. Phys. Lett.* **70**, 170.
Deeney, C. *et al.* (1995). *Phys. Rev. E* **51**, 4823.
Deeney, C. *et al.* (1997*a*). *Phys. Rev. E* **56**, 5945.
Deeney, C. *et al.* (1997*b*). *Rev. Sci. Instr.* **68**, 653.
Deeney, C. *et al.* (1998). *Phys. Rev. Lett.* **81**, 4883.
Douglas, M.R. *et al.* (1997*a*). *Phys. Rev. Lett.* **78**, 4577.
Douglas, M.R. *et al.* (1997*b*). *Bull. Am. Phys. Soc.* **42**, 1878.
Douglas, M.R. *et al.* (2000). *Phys. Plasmas* **7**, 1935.
Farley, D.R. *et al.* (1999). *Phys. Rev. Lett.* **83**, 1982.
Golberg, S.M. & Velikovich, A.L. (1993). *Phys. Fluids B* **5**, 1164.
Golub, T.A. *et al.* (1999). *Appl. Phys. Lett.* **74**, 3624.
Haines, M.G. (1998). *IEEE Trans. Plasma Sci.* **26**, 1275.
Hammer, J.H. & Ryutov, D.D. (1999). *Phys. Plasmas* **6**, 3302.
Hammer, J.H. *et al.* (1996). *Phys. Plasmas* **3**, 2063.
Kalantar, D. & Hammer, D. (1993). *Phys. Rev. Lett.* **71,** 3806.
Katzenstein, J. (1981). *J. Appl. Phys.* **52**, 676.
Lebedev, S.V. *et al.* (1998). *Phys. Rev. Lett.* **81**, 4152.
Lebedev, S.V. *et al.* (1999). *Phys. Plasmas* **6**, 2016.
Lebedev, S.V. *et al.* (2000*a*). *Phys. Rev. Lett.* **84**, 1708.
Lebedev, S.V. *et al.* (2000*b*). *Phys. Rev. Lett.* **85**, 98.
Lebedev, S.V. (2001). *Astrophysical Journal* (in press).
Lindemuth, I.R. (1990). *Phys. Rev. Lett.*, **65**, 179.
Matzen, M.K. (1997). *Phys. Plasmas* **4**, 1519.
Mitchell, I.H. *et al.* (1996). *Rev. Sci. Instrum.* **67**, 1533.
Mosher, D. *et al.* (1998). *Bull. Am. Phys. Soc.* **43**, B1F3.
Nash, T.J. *et al.* (1999). *Phys. Plasmas* **6**, 2023.
Olson, R.E. *et al.* (1999) *Fusion Technol.* **35**, 260.
Peterson, D.L. *et al.* (1999). *Phys. Plasmas* **6**, 2178.
Pikuz, S.A. *et al.* (1999). *Phys. Rev. Lett.* **83**, 4313.
Ruiz-Camacho, J. *et al.* (1999). *Phys. Plasmas* **6**, 2579.
Ryutov, D.D. *et al.* (2000). *Rev. Mod. Physics* **72**, 167.
Sanford, T.W.L. *et al.* (1996). *Phys. Rev. Lett.* **77**, 5063.
Sanford, T.W.L. *et al.* (1998). *Phys. Plasmas* **5**, 3737.
Shelkovenko, T.A. *et al.* (1999). *Rev. Sci. Instrum.* **70**, 667.
Sinars, D.B. *et al.* (2000). *Phys. Plasmas* **7**, 1555.
Spielman, R.B. *et al.* (1997). *Rev. Sci. Instrum.* **68**, 782.
Spielman, R.B. *et al.* (1998). *Phys. Plasmas* **5**, 2105.
Terry, R. *et al.* (1999). *Phys. Rev. Lett.* **83**, 4305.
Whitney, K. *et al.* (1997). *Phys. Rev. E* **56**, 3540.
Yadlowsky, E.J. *et al.* (1996). *Phys. Plasmas* **3**, 1745.